UNIVERSITY OF CALIFORNIA SAN DIEGO

A Joint Seismic and Space Geodetic Investigation of the 2016 Lamplugh Glacier and 2017 Wrangell Mountains (Alaska) Landslides

A thesis submitted in partial satisfaction of the requirements
for the degree Master of Science

in

Earth Sciences

by

Xinyu Luo

Committee in charge:

Professor Wenyuan Fan, Chair
Professor Yuri Fialko
Professor Peter M. Shearer

2022

The thesis of Xinyu Luo is approved, and it is acceptable in quality and form for publication on microfilm and electronically.

University of California San Diego

2022

TABLE OF CONTENTS

LIST OF FIGURES

LIST OF TABLES

ACKNOWLEDGEMENTS

I want to acknowledge Assistant Professor Wenyuan Fan for his support as my advisor and chair of my committee. His diligent attitude toward science is impressive, and he is always available for discussion whenever I need help during my research. His pursuit of excellence and attention to details in scientific research is inspiring. His guidance and teaching will continue to inspire me in my future career.

I want to thank Professor Yuri Fialko for his guidance on the geodetic part of my research paper. With his guidance and teaching, I was able to learn knowledge entirely new for me and apply it to my research. I want to thank Professor Peter M. Shearer for his support of being on my committee and provide guidance. His keen observation and approaches to problems are qualities I need to continually work on to improve. I want to thank all professors who taught me during these two years.

I want to thank my cohorts. Their help during my research is invaluable. It is my fortune to be able to meet my cohorts here, learn from them and eventually become their friend during my study here. I also want to thank everyone I have met or who helped me during my study here. You light up my life during this pandemic period.

Lastly, I want to thank my parents for their constant support.

The thesis, in full, has been submitted for publication of the material as it may appear in the Journal of Geophysical Research-Earth Surface: Luo, X., Fan, W., and Fialko, Y., A joint seismic and space geodetic investigation of the 2016 Lamplugh Glacier and 2017 Wrangell Mountains (Alaska) landslides, submitted. I am the primary investigator and author of the paper.

ABSTRACT OF THE THESIS

A Joint Seismic and Space Geodetic Investigation of the 2016 Lamplugh Glacier and 2017 Wrangell Mountains (Alaska) Landslides

by

Xinyu Luo

Master of Science in Earth Sciences

University of California San Diego, 2022

Professor Wenyuan Fan, Chair

Landslides commonly occur in areas with steep topography and abundant precipitation, and can pose a significant hazard to local communities. Some of the largest known landslides occurred in Alaska, including several that caused local tsunamis. Many more landslides may have gone undetected in remote unpopulated areas due to lack of observations. In this study, we develop an integrated procedure based on seismic and geodetic observations to detect, locate, validate, and characterize landslides in Alaska. Seismic observations have shown promise in continuously monitoring landslide occurrence, while remote sensing techniques are well suited for verification

and high-resolution imaging of the detected landslides. We validate our procedure using data from the previously detected June 28, 2016, Lamplugh Glacier landslide. We also present observations of a previously unknown landslide that occurred on September 22, 2017 in the Wrangell Mountains region. The Wrangell Mountains landslide generated a coherent surface wavefield recorded across Alaska and the contiguous US. We used Sentinel-1 Synthetic Aperture Radar and Sentinel-2 optical imagery to map the respective mass deposit. To investigate the landslide dynamics, we inverted regional seismic surface wave data for a centroid single force failure model. Our model suggests that the Wrangell Mountains landslide lasted for about 140 s and had two subevents involving at least five distinct episodes. We estimate that the landslide had displaced 3.1–13.4 million tons of rocks over a distance of $\sim$2 km. Our results suggest that combining seismic and geodetic observations can vastly improve the detection and characterization of landslides in remote areas in Alaska and elsewhere, and providing new insights into the landslide dynamics.

Chapter 1

Introduction

Landslides can denude mountains, transport sediments to fluvial networks, and impact regional ecosystems by drastically changing the landscape (e.g., Benda and Dunne, 1997; Gomi et al., 2002; Korup, 2005; Imaizumi and Sidle, 2007). Landslides involve hydromechanical processes that move rocks and sediments downhill, driven by gravitational forces (e.g., Gomberg et al., 1995; Milillo et al., 2014; Fan et al., 2017). A broad range of mass wasting events can be categorized as landslides, such as debris flows, lahars, slope creep, and avalanches (e.g., Iverson et al., 2000; Allstadt, 2013; Delbridge et al., 2016; Lai et al., 2018). Such events can last from minutes to years (e.g., Ekström and Stark, 2013; Gualtieri and Ekström, 2018; Hu et al., 2019), and result in significant damage and casualties (Petley, 2012; Hibert et al., 2015; Froude and Petley, 2018). In addition to mass wasting, landslides that occur near bodies of water may produce local tsunamis and further endanger local communities (Bardet et al., 2003; Dufresne et al., 2018). Despite much progress

made toward understanding of landslides and the associated hazards, a number of questions remain, largely due to a lack of systematic characterization of the principal physical parameters of landslides such as their location, time, volume, and sliding speed (Ekström and Stark, 2013; Mondini et al., 2021).

It is challenging to continuously monitor landslides in remote regions because conventional methods such as field and aerial surveys are costly and time-consuming, and typically limited to case studies (Guthrie et al., 2012; Dufresne et al., 2019; Toney et al., 2021). Due to the challenging terrain conditions, field investigations of Alaska landslides are infrequent and have been mainly conducted in coastal regions (Hibert et al., 2015). For this reason, relatively few landslides have been reported in Alaska (Kirschbaum et al., 2015; Bahavar et al., 2019), despite the fact that they include some of the largest landslides observed in the US. For example, the 2015 Taan Fjord landslide near Icy Bay mobilized 180 million tons of rocks and produced a local tsunami reaching as high as 193 m (Higman et al., 2018). As slope failure occurrence correlates with the topographic relief in mountainous areas (Korup et al., 2007), landslides likely occur frequently in Alaska without being detected (Kirschbaum et al., 2015).

Remote sensing methods, such as Synthetic Aperture Radar (SAR), have been increasingly exploited to study landslides (Fruneau et al., 1996; Singhroy et al., 1998; Colesanti and Wasowski, 2006). For example, SAR can directly image the surface disturbance due to landslides at a high spatial resolution by comparing the image amplitude changes or phase coherence between radar acquisitions taken before and after an event (e.g., Mondini et al., 2021). Additionally, satellite or aerial optical

imagery can provide ground-truth observations to determine exact landslide location, composition, area, and runoff distance (Lacroix et al., 2018; Dufresne et al., 2019; Qu et al., 2021). However, due to infrequent acquisitions, exact timing of landslides and details of their initiation cannot be solely resolved using space geodetic observations (Mondini et al., 2021).

One additional method to study landslide is through seismology method because landslide can generate seismic signals (Kanamori and Given, 1982; Kawakatsu, 1989a; Brodsky et al., 2003). Fast-moving landslide can generate seismic signals on two scales: short-period(few seconds to tens of Hz) (Hibert et al., 2011; Yamada et al., 2012; Doi and Maeda, 2020) to intermediate and long period(10s-150s) (Moretti et al., 2012; Allstadt, 2013; Ekström and Stark, 2013; Li et al., 2019). The short-period seismic signals are generated at small scale such as impacts of individual blocks, frictional process or due to small-scale topography features (Huang et al., 2007; Schneider et al., 2010). The coherent long-period waveforms at intermediate to long periods generated by the process of loading and unloading of the ground associated with the deceleration and acceleration of the sliding mass, and they can be modeled as centroid single force(CSF) (Kawakatsu, 1989a; Kanamori and Given, 1982).

Seismic observations have shown promise in detecting and locating landslides (Ekstrom, 2006; Dammeier et al., 2016; Manconi et al., 2016; Fan et al., 2018) and resolving landslide dynamics (Kanamori and Given, 1982; Brodsky et al., 2003; Poli, 2017; Lai et al., 2018; Intrieri et al., 2018). The short-periods seismic wave from landslide typically builds up gradually and taper off slowly in the end and therefor shows

a spindle shape (Deparis et al., 2008; Hibert et al., 2011). The short-period seismic wave has been observed for landslides of all scales. However, the high frequency attenuate fast so it is only applicable at local or regional distance. On the other hand, the intermediate to long period seismic waves can often be observed globally and have been used to study landslide occurrence in remote regions(Ekstrom, 2006; Fan et al., 2018; Okuwaki et al., 2021). Seismic observations have also shown promise in resolving landslide dynamics. Previous research have used intermediate and long periods seismic signals to study landslide processes using CSF model(Allstadt, 2013; Gualtieri and Ekström, 2017; Okuwaki et al., 2021). The sliding mass, trajectory, speed, and friction coefficient can be determined with the help of geodetic constrain. The seismic records have a high temporal resolution and may be used to continuously monitor landslides, complementing the space geodetic observations (e.g., Fan et al., 2018; Okuwaki et al., 2021).

Here we develop an integrated approach combining space geodetic and seismic observations to detect and locate Alaska landslides, and further use the suite of geophysical observations to infer landslide failure processes. We first apply the method to the well-documented 2016 Lamplugh Glacier landslide (Bessette-Kirton et al., 2018; Coe et al., 2018; Dufresne et al., 2019) to verify our procedure. We then use our method to identify a previously unknown landslide that occurred on September 22, 2017 in the Wrangell Mountains region in Alaska. As we demonstrate below, the 2017 Wrangell Mountain landslide had two subevents and a multiple-episode failure process. The results demonstrate the effectiveness of the procedure and offer new insights into failure dynamics of complex landslides in Alaska.

Chapter 2

Data

2.1 Seismic Data

We use continuous, vertical-component, broadband seismic data to locate landslides with stations registered at the International Federation of Digital Seismograph Networks (FDSN) (Figure 2.1). The data were downloaded from the Data Management Center (DMC) of the Incorporated Research Institution for Seismology (IRIS). The original records are sampled at 1 Hz, and we bandpass-filtered them in the 20 to 50 s period band using a fourth-order Butterworth filter.

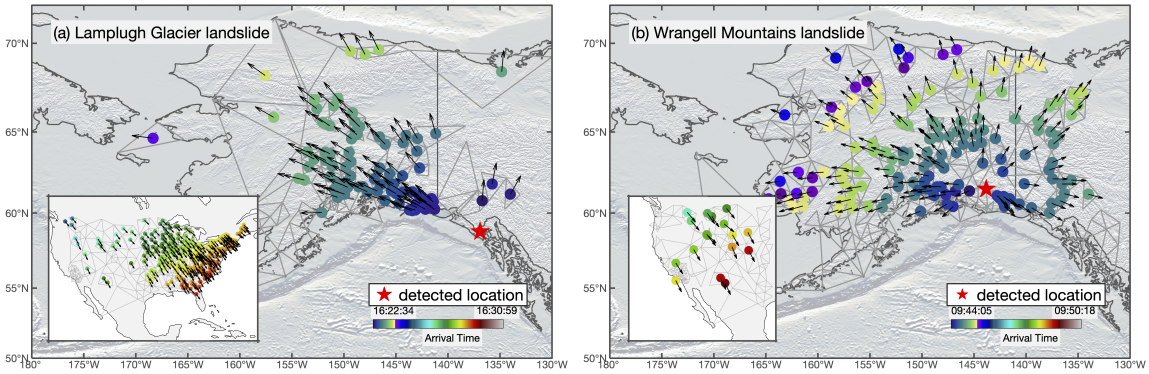

Figure 2.1: Rayleigh wavefields of the June 28, 2016 Lamplugh Glacier landslide (a) and the September 22, 2017 Wrangell Mountains landslide (b). Surface wave propagation directions and arrival times are shown as the arrows and dots respectively. Triad subarrays are shown as gray triangles. Red stars are the seismically resolved locations. Insets show wavefields in the contiguous US.

To investigate the landslide failure dynamics, near-field to regional-distance seismic records are used for inverting centroid single force (CSF) models of the landslides (Figure 2.2–4.5). We use three-component, broadband displacement records from stations within five degrees of the landslide location to invert for the CSF models. The records are sampled at 40 or 50 Hz, and we fit waveforms in a 200 s long time window around the surface waves. Assuming an apparent moveout velocity of 3.7 km/s, the time window is selected as 40 s before and 160 s after the predicted arrival time, and the waveforms are tapered before being used for the CSF inversion. Additionally, we inspect high-frequency radiation of near-field stations (Figure 2.2 and 4.1) to infer the nature of the seismic sources.

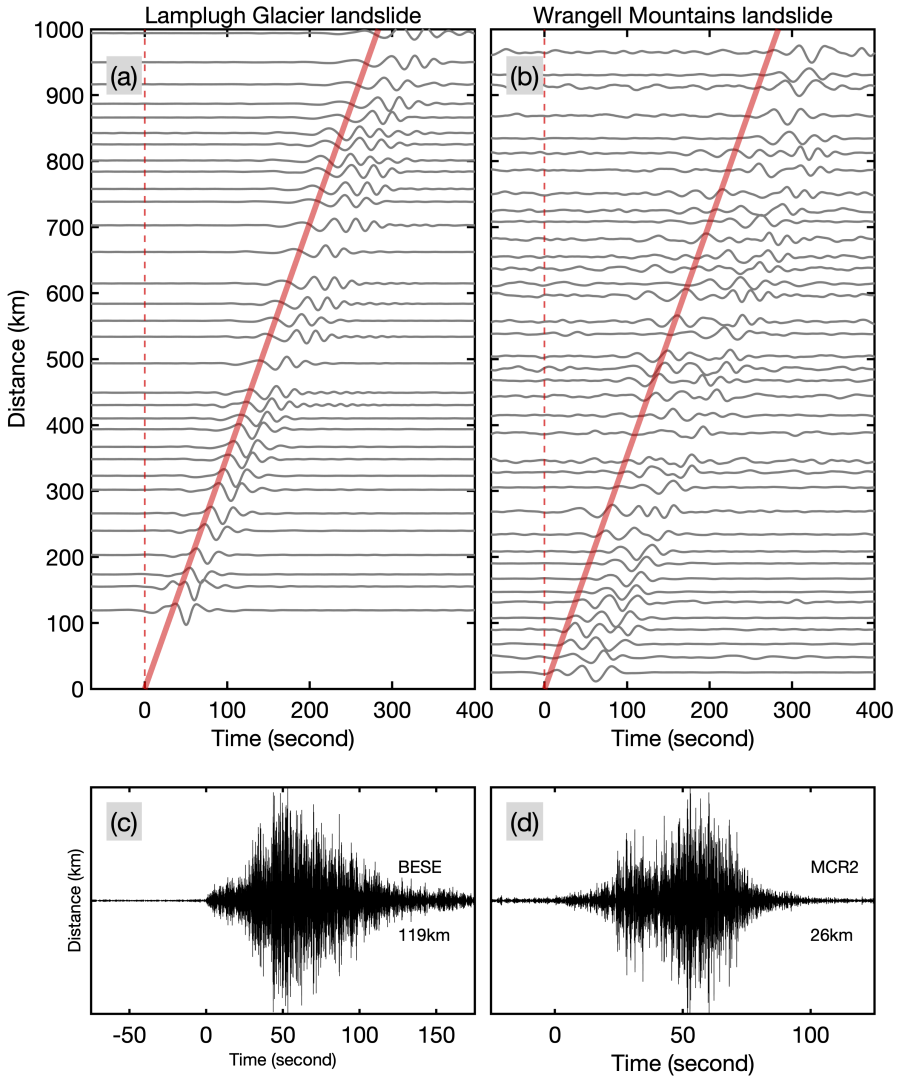

Figure 2.2: Record sections that are aligned using the seismically resolved locations in Figure 2.1. Records are self-normalized and bandpass-filtered to show signals in the 20–70 s period band. Red lines show a 3.6 km/s reference move-out velocity. Origin time (0 s) denotes 16:20:53 (UTC) for the Lamplugh Glacier landslide and 09:43:11 (UTC) for the Wrangell Mountains landslide. (a), Vertical record section of the June 28, 2016 Lamplugh Glacier landslide . (b), Vertical record section of the September 22, 2017 Wrangell Mountain landslide. (c), Vertical high-frequency record (0.1 to 1 s period) of the 2016 Lamplugh Glacier landslide at the nearest station BESE (119 km away). (d), Vertical high-frequency record (0.1 to 1 s period) of the 2017 Wrangell Mountain landslide at the nearest station MCR2 (26 km away).

2.2 Space Geodetic Data

We use the Sentinel-2 optical imagery to confirm whether the seismically detected sources are indeed associated with landslides (Figure 4.8). The optical images are downloaded from Copernicus Open Access Hub of the European Space Agency. We use images from bands 2, 3, and 4 of the Multispectral Instrument on board of the Sentinel-2A and Sentinel-2B satellites to generate a true color composite of the regions of interest. In addition to the optical imagery, we use Synthetic Aperture Radar (SAR) data from Sentinel-1A satellite (Figures 4.7 and 4.9). The SAR data offer independent confirmation and validation of the events and are highly complementary to the Sentinel-2 optical imagery. The data were processed using GMTSAR (Sandwell et al., 2011). We calculate the radar amplitude for each acquisition date, and coherence of the interferometric phase. Both the phase coherence and variations in the radar amplitude can carry information about surface changes caused by the landslides.

Chapter 3

Methods

3.1 Detecting Landslides Using Coherent Seismic Surface Wavefields

We use AELUMA (Automated Event Location Using a Mesh of Arrays) to detect and locate Alaska landslides (de Groot-Hedlin and Hedlin, 2015; Fan et al., 2018). The method uses surface waves recorded by large aperture arrays to identify seismic sources. It first detects coherent surface wave signals using subarrays and then assembles the measured surface wave arrival angles to locate the seismic sources, assuming that the waves propagate along great circle paths (Fan et al., 2018). In practice, we first divide the large arrays into non-overlapping three-station subarrays (triads). Each triad is required to have internal angles between 30–120° to reliably resolve the arrival angles. Next, beamforming analysis is applied to band-passed filtered (20–50 s) continuous data to detect coherent signals. We use a 600 s long sliding time

window and a 300 s increment step to examine the data. The beamforming analysis is applied to each triad and time window independently. The detections are screened through a quality control procedure, such as examining the average cross-correlation coefficient, local phase velocity, and beam-power value of each detection (Fan et al., 2018). The remaining ones are used for association, which are grouped into non-overlapping clusters. Each cluster is then used to locate one seismic source, and its location uncertainty is empirically estimated by examining the spatial structure of grids within a pre-defined misfit threshold (de Groot-Hedlin and Hedlin, 2018; Fan et al., 2018, 2020). Finally, the quality of each located seismic event is assessed to avoid duplicates and a catalog is populated. The approach is data-driven, makes few assumptions about the nature of the seismic sources, and does not need a velocity model (Fan et al., 2018). The method is particularly well-suited for detecting unconventional seismic sources such as landslides that are commonly missed in standard catalogs (Fan et al., 2019; Okuwaki et al., 2021; Fan et al., 2020).

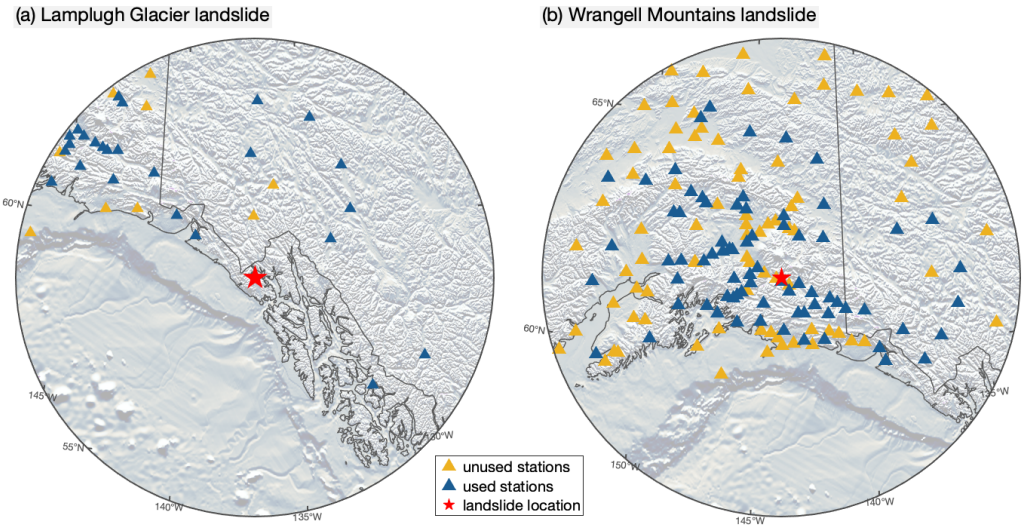

Figure 3.1: Stations used for centroid single force (CSF) inversions. (a), Lamplugh Glacier landslide. (b), Wrangell Mountains landslide. Red stars show seismic locations of landslides. Blue triangles indicate the stations used in the CSF inversion. Yellow triangles indicate the stations that are within the five-degree searching range but are not selected for inversions.

3.2 Centroid Single Force Inversion

The acceleration and deceleration of a landslide moving downhill is expected to impose shear tractions at the sliding interface, which can be approximated as centroid single forces (CSF; Kawakatsu, 1989b; Kanamori and Given, 1982). The sliding process can generate broadband seismic surface waves propagating up to thousands of kilometers if the landslide couples with solid Earth and does not significantly disintegrate (Fukao, 1995; Allstadt, 2013). The CSF models can offer high-resolution insights into the landslide failure process and characteristics (e.g., Allstadt, 2013). Here we use regional three-component broadband seismic records to invert for CSF

models of the 2016 Lamplugh Glacier and 2017 Wrangell Mountains landslides (Figure 4.2). We use a frequency-domain inversion method derived from (Fan et al., 2014), which was initially designed for finite-fault slip inversion. We apply the inversion scheme iteratively to update the model by gradually including usable traces within five degrees of the landslides.

The landslide displacement waveforms are convolutions between the CSF model and the Green's functions for a given source-receiver pair. In the frequency domain, the displacement spectra are linearly related to the CSF spectra (Equation 3.1), which can be inverted for each frequency bin independently. In a discrete format, the linear relation can be written as

$$u_n(\underline{x}, \omega) = G_{ni}(\underline{x}, \omega) F_i(\omega), \tag{3.1}$$

where u_n, G_{ni}, and F_i are the spectra of the displacement seismogram, Green's function, and CSF; ω is the angular frequency; x denotes the relative locations between the source and receiver; and n and i are the receiver- and source-side directions, respectively. The failure history of a CSF model is then obtained from the inverse Fourier transform of its estimated spectra. The zero-frequency spectra are set as zero to ensure that the net forces are zero. We minimize ℓ_1 data misfit in the inversion (Equation 3.2) to obtain robust models, and the procedure is effective when using a large number of stations with observation outliers:

$$\mathbf{F} = \arg\min \|\mathbf{u} - \mathbf{G} \cdot \mathbf{F}\|_1. \tag{3.2}$$

The Green's function is obtained using the Instaseis method (van Driel et al., 2015), which extracts Green's functions from a pre-computed database that is computed using the axisymmetric spectral-element method (Nissen-Meyer et al., 2014). The ℓ_1 inverse problem is solved using convex optimization (CVX package; Grant and Boyd, 2014, 2008).

In practice, the seismic data are first detrended, and the instrument response is removed. We invert CSF spectra in the 20–70 s period band (0.014–0.02 Hz) after applying a Tukey taper with a cosine fraction of 15% to the 200 s long records. We gradually include all usable data and iteratively update the CSF model. We first manually select a set of seismic traces to obtain an initial model, and traces are selected to have clear event signals and low background noise. With the initial model, we forward compute synthetic waveforms at all stations for all three components. The synthetic waveforms ($\mathbf{u}^s$) are cross-correlated with the observations, and the normalized residual are computed for each trace. Here the normalized residual is defined as $\|\mathbf{u} - \mathbf{u}^s\|_1 / \|\mathbf{u}\|_1$ using the ℓ_1 misfit. Traces with cross-correlation (CC) coefficients above a threshold of 0.6 and normalized residual below a threshold of 0.7 are included to invert for a new CSF model. Such an inversion-update procedure is repeated until no new traces can be added to update the model. The procedure typically converges within three iterations.

Further, the cross-correlation during the iteration step would measure delay times that can be used to empirically shift the traces before the next iteration. Applying the time correction would reduce impacts from heterogeneous three-dimensional (3D) velocity structures in Alaska (Jiang et al., 2018; Feng and Ritzwoller, 2019; Nayak

et al., 2020). To quantify the uncertainties of the obtained CSF models, we bootstrap the set of traces that are used to obtain the final preferred models. In each bootstrap run, we randomly draw 80% of the total traces for the 2016 Lamplugh Glacier and 2017 Wrangell Mountains landslides respectively (Figure 4.4), and the same traces can be selected multiple times for a realization. We perform 500 bootstrap realizations for each landslide to obtain statistically reliable estimates of the model uncertainties.

3.3 Validating and Characterizing Landslides Using Space Geodetic Imagery

3.3.1 Sentinel-2 Optical Imagery

The Sentinel-2 imagery provide 10 m-resolution, true-color composite of the areas of interest. We initially select two images that most tightly bracket the event date and have a minimal cloud coverage to examine the source region. When needed, we also use additional images taken during different seasons to confirm the nature of seismically detected events (e.g, discriminate landslides and snow avalanches). The optical imagery is further used to estimate the landslide area and runout distance. The runout distance helps constrain the mass of the landslide material and can be also compared to the displacement inferred from the CSF model (Figure 4.5).

3.3.2 Sentinel-1 SAR Imagery

We also use Sentinel-1 SAR data to independently classify the seismic detection and characterize the landslide parameters by examining the phase coherence and variations in the radar amplitude in the radar images taken before and after the event (Yonezawa and Takeuchi, 2001; Mondini et al., 2021). Unlike Sentinel-2 optical imagery, Sentinel-1 radar imagery is not limited by weather and light conditions (Rees, 2013). Ground motion due to a landslide can cause changes in the reflective properties of the Earth's surface, which can be manifested in variations in the radar amplitude and phase correlation. Anomalous changes in the radar amplitude can be used to map the landslide extent (Mondini et al., 2021). We focused the raw SAR data into Single Look Complex (SLC) images, and computed the radar amplitude images for each acquisition date. Images were co-registered using the BESD (Bivariate Enhanced Spectral Diversity) algorithm (Wang et al., 2017). We then subtracted the co-registered amplitude images to obtain the differential amplitude. We also computed phase coherence for each interferometric pair spanning the event date. Phase coherence is another measure of surface changes that can be used to map out the landslide area. All of the above steps are automated and can be readily applied to process SAR data covering large areas.

Chapter 4

Results

We first use data from a known landslide to validate our integrated detection procedure. Our test case is the 2016 Lamplugh Glacier landslide that occurred in Alaska.

4.1 The Lamplugh Glacier Landslide

The Lamplugh Glacier landslide generated globally detectable surface waves (Ekstrom, 2006; Ekström et al., 2012). The landslide lasted 75 s, and occurred in two stages, with a total displacement of about 10 km (Dufresne et al., 2019). The event mobilized 1.4×10^{11} kg of materials. The 2016 Lamplugh Glacier landslide produced a coherent surface wavefield across Alaska and the contiguous US (Figure 2.1a). Rayleigh waves can be easily identified from vertical velocity records that are filtered at 20–70 s period band, and the waveforms remain coherent up to 1000 km away (Figure 2.2a). The event was detected by 257 triad subarrays from 354 stations. Our

seismically inferred event location is 3 km away from the true landslide location. The nearest station, BESE, is 119 km away from the landslide, and its high-frequency record (0.1–1 s period band, vertical component) has a spindle shape without clear body wave phases (Figure 2.2c), which is typical for landslides. Additionally, the spectrum of BESE has a bell shaped spectrum (Figure 4.1a) with the first 30 s exhibiting limited high-frequency radiation, differing from typical earthquake seismograms (e.g., Gualtieri and Ekström, 2018). There is more high-frequency radiation 30 s after the event onset, which may be due to changes in the speed of the mobilized material (Norris, 1994; Deparis et al., 2008; Dammeier et al., 2011; Hibert et al., 2011).

As a validation of our CSF inversion approach, we estimate a failure model of the 2016 Lamplugh Glacier landslide using 45 traces from 25 stations (Figure 3.1b). The CSF model suggests that the event had two downward acceleration stages and two associated deceleration stages (Figure 4.3a–c). The landslide primarily slid towards north as suggested by the horizontal accelerations (Figure 4.5a), consistent with satellite imagery (Figure 4.7b) (Dufresne et al., 2019). The peak centroid force is 2.55×10^{11} N, which empirically corresponds to a displaced mass of 1.34×10^{11} kg (Ekström and Stark, 2013). This mass estimate agrees well with the field survey estimate of 1.41×10^{11} kg (Dufresne et al., 2019). The preferred CSF model can explain the seismic observations well, including traces that are not used in the CSF inversion (example traces in Figure 4.2a–c, see all traces in Figure B.1). The CSF model is robustly resolved as the ensemble of bootstrap models does not deviate away from the preferred model very much (grey lines in Figure 4.3a–c). For each bootstrap realization, we record the normalized residual and cross-correlation (CC)

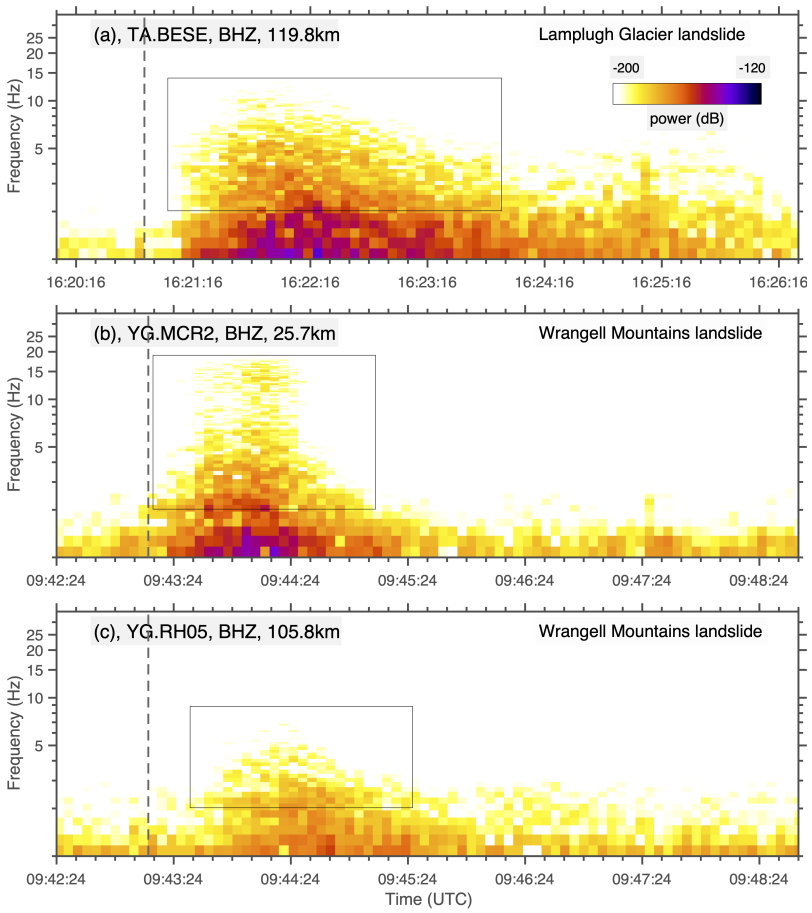

Figure 4.1: Spectrograms of vertical component at BESE (a) for the 2016 Lamplugh Glacier landslide and at MCR2 (b) and RH05 (c) for the 2017 Wrangell Mountain landslide. Gray boxes show the part where the stations have recorded high frequency(>1 Hz) radiation.

coefficient of each waveform, and the median values of the CC coefficient and the median values of the residuals are around 0.6 and 0.65 for all three components, respectively (Figure 4.4a and c).

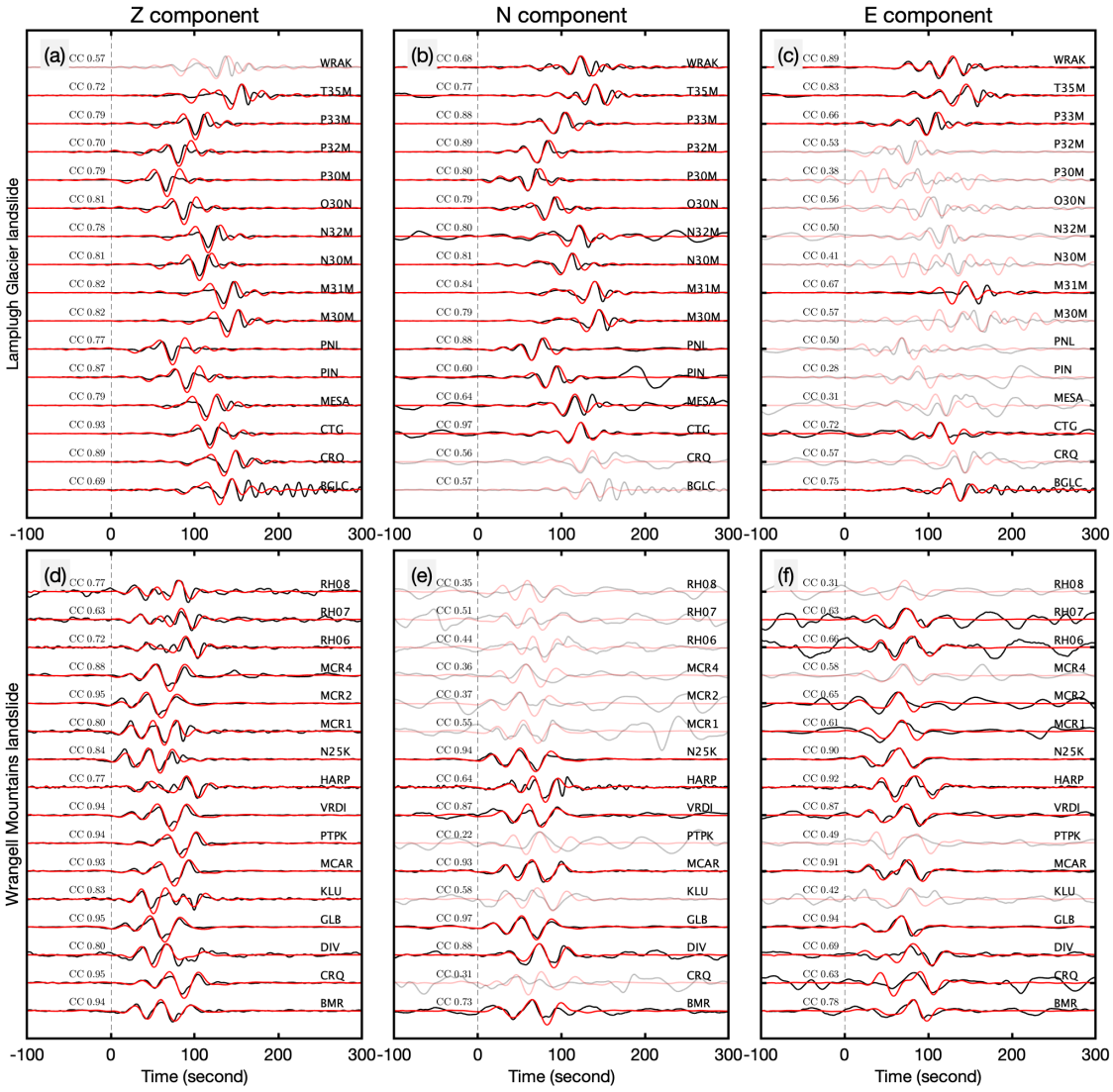

Figure 4.2: Example waveforms of the landslides. (a–c), Observed and synthetics seismograms of the June 28, 2016 Lamplugh Glacier landslide. (d–f), Observed and synthetics seismograms of the September 22, 2017 Wrangell Mountains landslide. Black and red traces are observed and synthetic seismograms, respectively. Opaque traces were not used for the centroid single force inversion. Origin times (0 s) are the onset times of the 200 s time windows. All traces used in the inversion are shown in Figure B.1–B.4.

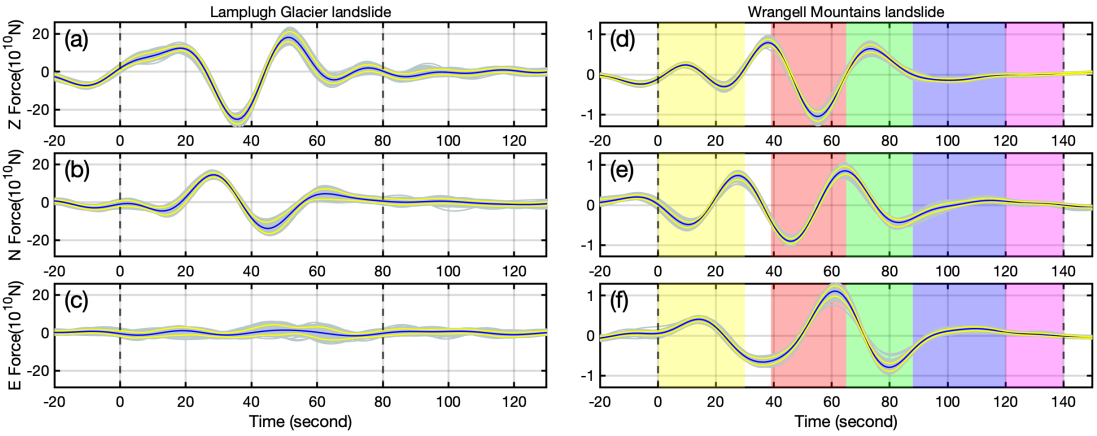

Figure 4.3: Three-component centroid single force (CSF) models of the 2016 Lamplugh Glacier landslide (a–c) and the 2017 Wrangell Mountains landslide (d–f). Blues lines show the preferred CSF models. Gray lines show CSF models obtained from the bootstrap resampling. Yellows lines show the 90% confidence intervals inferred from bootstrap resampling. Dash lines indicate the estimated origin and ending times of the landslides. Color patches in (d–f) sequentially show five stages of the 2017 Wrangell Mountains landslide.

The 2016 Lamplugh Glacier landslide gave rise to conspicuous changes in the back-scatter characteristics of the landslide area, expressed in changes in the radar amplitude. For the 2016 Lamplugh Glacier landslide, we use data acquired on June 6 and June 30, 2016 by the Sentinel-1A satellite from the descending track 145 (absolute orbits 11592 and 11942) in the Interferometric Wide(IW) swath mode (Figure 4.7). Figure 4.7a shows the amplitude of the Sentinel-1 radar image acquired on June 6, 2016, and Figure 4.7b shows the differential amplitude between the June 6 and June 30 acquisitions. As one can see in Figure 4.7b, the Earth's surface was roughened within the landslide area, resulting in an increased backscatter. The respective changes in the radar amplitude are not correlated with the pre-event radar amplitude (Figure 4.7a). The phase coherence from the same interferometric pair is

unfortunately less useful in this case (Figure 4.6) because of a substantial snow cover that degraded the phase coherence over the entire scene. The differential amplitude data suggest that the landslide had a runout of ∼10 km, moving northward. The area and boundary of the landslide inferred from the SAR images (Figure 4.7b) are consistent with results of previous studies which employed optical images and field surveys (Dufresne et al., 2019).

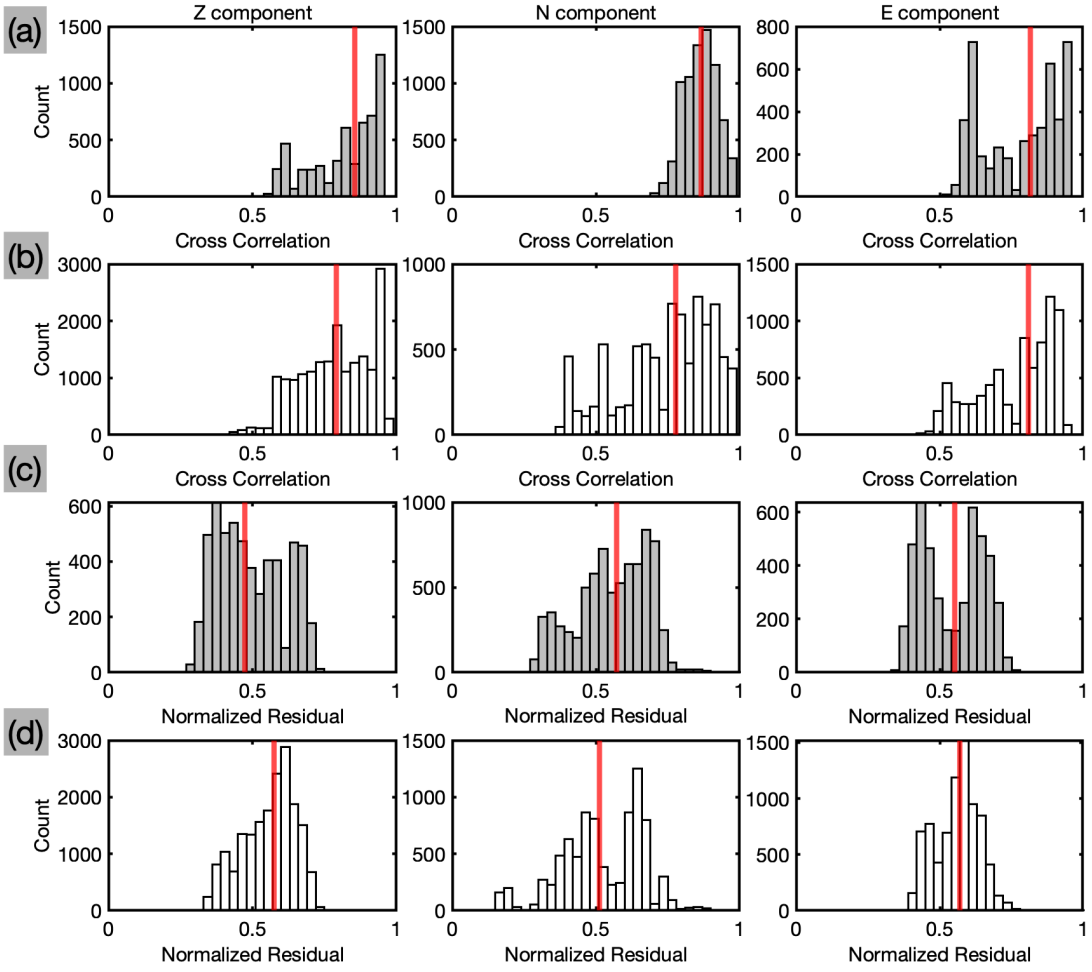

Figure 4.4: Histograms of the waveform residuals and cross-correlation coefficients from bootstrap realizations. (a) and (b), three-component cross-correlation coefficients of the observed and synthetic traces for the 2016 Lamplugh Glacier landslide and the 2017 Wrangell Mountains landslide, respectively. (c) and (d), three-component waveform residuals between the observed and synthetic traces for the 2016 Lamplugh Glacier landslide and the 2017 Wrangell Mountains landslide, respectively. Red lines denote the median values for each distribution.

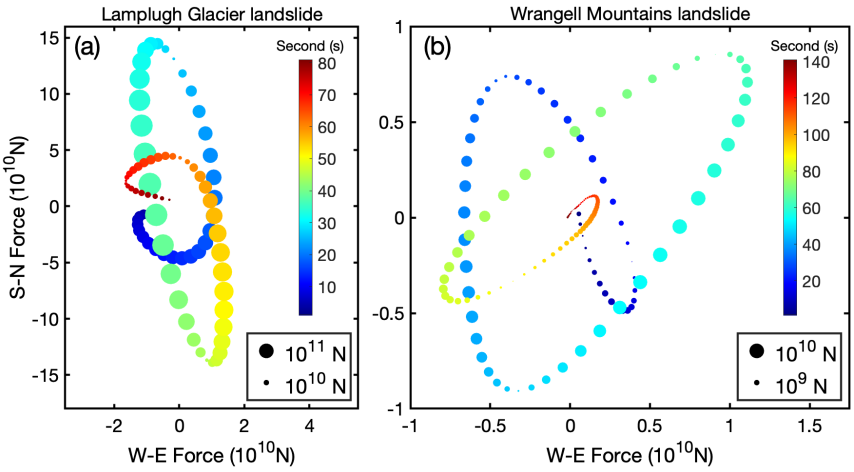

Figure 4.5: Horizontal centroid single force histories. (a), Lamplugh Glacier landslide. (b), Wrangell Mountains landslide. Color and size of the dots indicate the failure time and force strength.

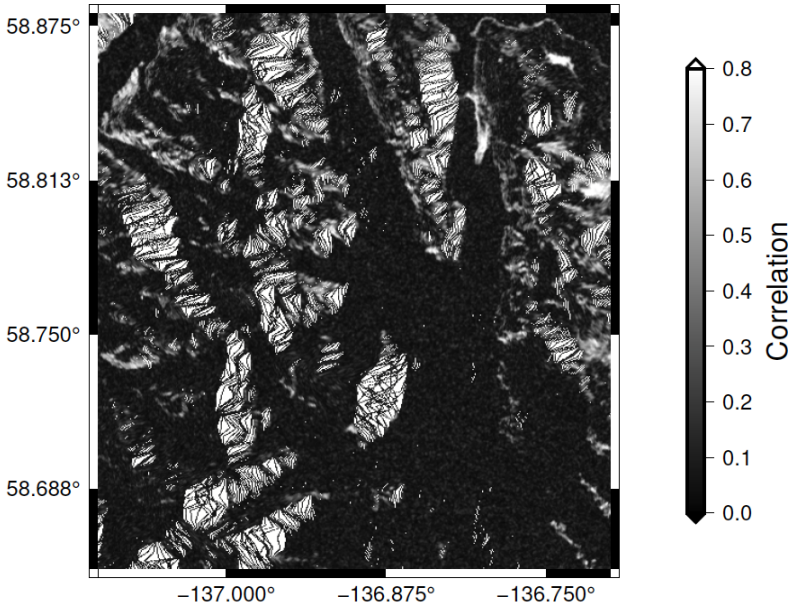

Figure 4.6: Sentinel-1 SAR correlation image obtained from two acquisitions on June 6 and June 30, 2017. The most of the area is decorrelated because of snow coverage in the region. So the changes due to the landslide is not visible.

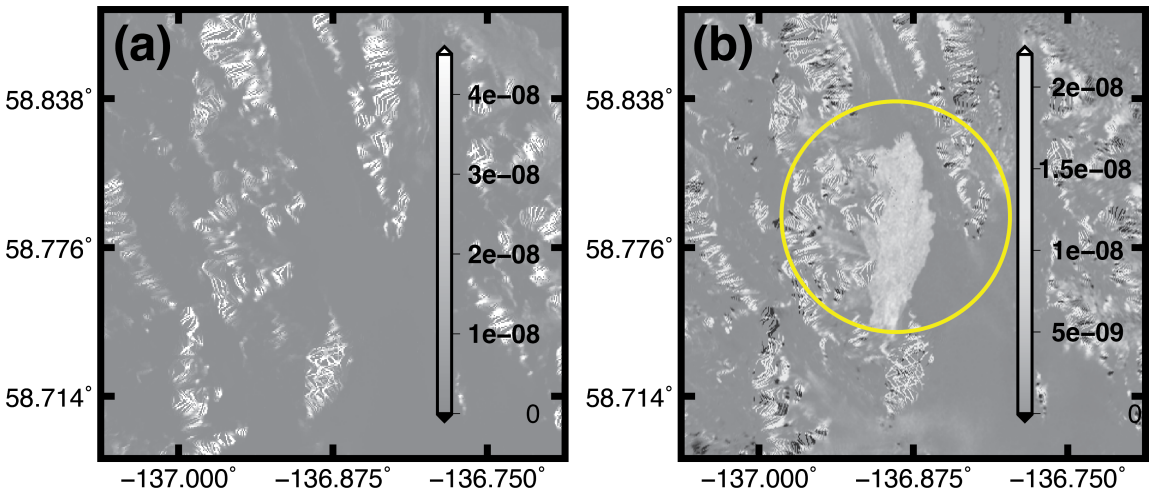

Figure 4.7: (a) Radar amplitude of a Sentinel-1 SAR image acquired on June 6 (before the 2016 Lamplugh Glacier landslide). (b) Differential radar amplitudes from two Sentinel-1 SAR images acquired on June 6 and 30. The 2016 Lamplugh Glacier landslide is outlined by the yellow circle, and manifested by an increased radar backscatter. The amplitude changes do not correlate with the local topography. Note the difference in color limits between the two panels.

4.2 The 2017 Wrangell Mountains Landslide

Here we report on a previously unregistered event in the Wrangell mountains region we discovered using the AELUMA method. The event occurred on September 22, 2017, and produced coherent waveforms that were detected by 162 triad subarrays from 238 stations in Alaska and the contiguous US (Figure 2.1b). We confirm that the event is a landslide by inspecting the Sentinel-2 images (Figure 4.8). Images from three acquisitions, dated August 5, 2017 before the seismically detected event, November 20, 2017 shortly after the event, and July 23, 2018 in the following summer, are used to investigate the Wrangell Mountains landslide (Figure 4.8). Ini-

tially, we used the the two Sentinel-2 images obtained on August 5 and November 20, 2017. These two images most tightly bracket the seismically detected event and are relatively cloud-free. Changes in surface conditions are obvious from a comparison of the two images (see areas outlined by yellow circles in Figure 4.8a–b). However, the November 20, 2017 acquisitions was affected by a snow cover (Figure 4.8b). To verify that the event was a landslide and not a snow avalanche, we inspected an image taken in the following summer (July 23, 2018, Figure 4.8c), and the landslide deposits can be clearly identified in the color composites in the image taken on July 23, 2018 (Figure 4.8c). The landslide deposits can be clearly identified in the color composites in the image taken on July 23, 2018 (Figure 4.8c). A comparison of Figure 4.8a and Figure 4.8c clearly shows the event was a landslide. The ground truth location obtained from Sentinel-2 imagery is 5 km away from the seismically determined location. The Sentinel-2 imagery also suggests that the landslide produced two deposit piles, with the greater pile having a runout distance of 1.5 km (Figure 4.8c). The surface area of the two piles is about 1.6 km^2 in total.

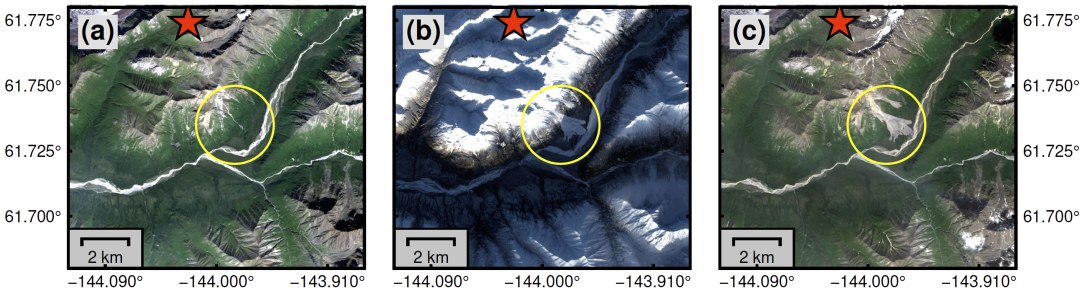

Figure 4.8: Sentinel-2 imagery of the 2017 Wrangell Mountains landslide. (a–c), Optical images acquired on August 5 and November 20, 2017, and July 23, 2018. Red star shows the seismically determined location. Yellow circle indicates surface alternation caused by a landslide. The images are true color composition using bands 2–4 of Sentinel-2. Color stretching is applied to adjust image brightness.

We also verified the landslide occurrence using SAR data that were acquired on September 20 and October 2, 2017 by the Sentinel-1A satellite from the descending track 14 (absolute orbits 18461 and 18636) in the IW swath mode (Figure 4.9). The 2017 Wrangell Mountains landslide is located at the intersection of the two sub-swaths (sub-swaths 2 and 3) of the Sentinel-1A track, and we used both sub-swaths in our analysis. The respective interferometric pair features a low phase coherence at the location suggested by the optical Sentinel-2 data. Because the location happens to be in the overlap area between two radar sub-swaths, the same low-coherence feature can be seen independently in each sub-swath (Figure 4.9). The radar amplitude also changes between the two acquisitions, with a higher backscatter anomaly at the landslide site (Figure 4.10). From the coherence images, the landslide area is estimated at ~ 1.7 km^2 using a coherence threshold of 0.15.

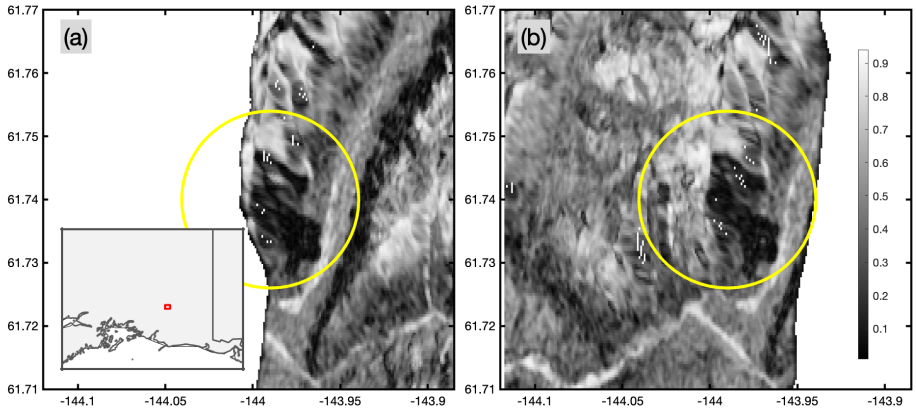

Figure 4.9: Sentinel-1 Phase coherence images obtained from two acquisitions on September 20 and October 2, 2017. (a) Sub swath 2. (b) Sub swath 3. Low coherence regions within the yellow circle correspond to the landslide area.

The landslide radiated seismic waves that can be clearly identified in the period band of 20–70 s up to 1000 km away (Figure 2.2b). The record section shows coherent wave packets with a moveout velocity of 3.6 km/s, which is consistent with typical surface wave velocity in the period band. Station MCR2 is 26 km away from the landslide (Figure 2.2d), which high-frequency (0.1–1 period band, vertical component) waveform has a spindle shape, confirming the source as a landslide. The high-frequency radiation lasted less than 100 s with two main episodes, and the second episode has a longer duration with greater amplitudes (Figure 2.2d). The spectrograms of the event (Figure 4.1b–c) are similar to that of the 2016 Lamplugh Glacier landslide in bell shapes (Deparis et al., 2008; Hibert et al., 2011). The seismic radiation above 5 Hz of the Wrangell Mountains landslide decayed rapidly at further distances (Figure 4.1c). Station RH05 is 106 km away from the Wrangell Mountains landslide, similar to the separation distance between BESE and the Lamplugh Glacier landslide, but its relative high-frequency content is significantly smaller compared to that of the Lamplugh Glacier landslide (Figure 4.1a,c).

The CSF model of the Wrangell Mountains landslide suggests a multi-episode failure process (Figure 4.3d–f), considerably more complex than that of the Lamplugh landslide. The model suggests a total duration of 140 s, which is 40 s longer than the high-frequency duration observed at MR2 (Figure 2.2d). Multiple acceleration and deceleration stages can be identified from the vertical centroid single force history (Figure 4.3d). The vertical force has a comparable peak amplitude as forces at horizontal directions, indicating three-dimensional sliding motions (Figure 4.3d–f). The horizontal force histories show that the Wrangell Mountains landslide may have

changed its sliding directions multiple times, different from the Lamplugh Glacier event, which mostly moved northward (Figure 4.5). The ensemble models from the bootstrap tests are tightly clustered around the preferred model (Figure 4.3d–f). Waveform ℓ_1 residuals and the cross-correlation coefficients from the bootstrap tests have a median CC value of 0.79 and a median residual value of 0.54 for the three components.

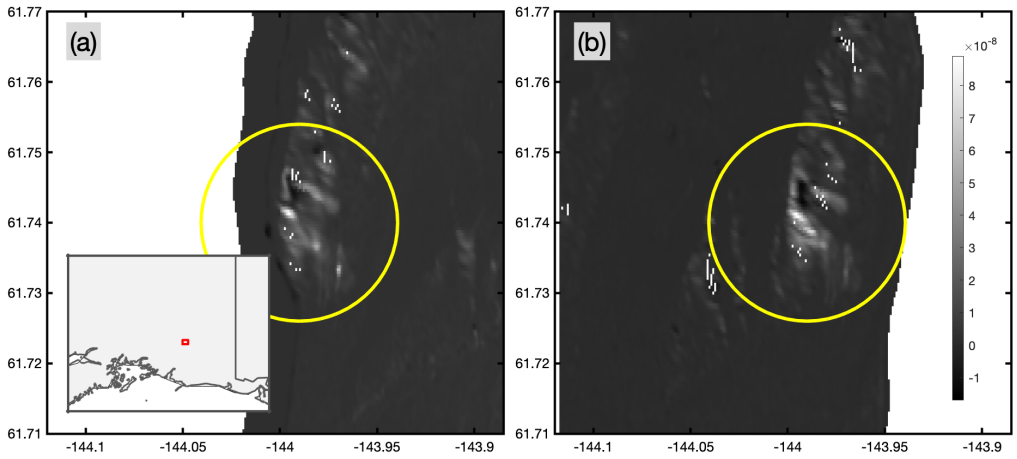

Figure 4.10: Differential radar amplitude calculated for two Sentinel-1 SAR images acquired before and after the 2017 Wrangell Mountains event. The yellow circles outlines areas of enhanced backscatter that does not correlate with local topogaphy. (a) differential amplitude for subswath 2. (b) differential amplitude for subswath 3.

Chapter 5

Discussion

5.1 Uncertainty and Resolution

The seismically resolved locations of the 2016 Lamplugh Glacier and 2017 Wrangell Mountains landslides are 3 km and, respectively, 5 km away from their ground-truth locations. Considering the wavelengths of the surface waves used in the AELUMA procedure, both cases are well resolved. Considering the wavelengths of the surface waves used in the AELUMA procedure, both cases are well resolved. The location accuracy is comparable to landslide relocation resolution obtained employing empirical Green's functions from ambient seismic noises Xie et al. (2020). Their spatial deviations are less than the grid separation distance (0.25°; Fan et al., 2018). The seismically resolved location may have uncertainties due to the relative positions between the array and the event, searching grid parameterization, and the 3D velocity anomalies in Alaska, which would cause surface-wave ray paths deviating away from

the great circle paths (Feng and Ritzwoller, 2019; Nayak et al., 2020). One way to evaluate the impacts of these factors is to examine the spatial structure of the searching grids that have misfit values within 125% of the minimum misfit (de Groot-Hedlin and Hedlin, 2018; Fan et al., 2018, 2020). The distance covariance matrix of the grids can be used to provide a formal way to examine the location uncertainties. We find that the 2016 Lamplugh Glacier landslide and the 2017 Wrangell Mountains landslide have maximum spatial uncertainties of 227 km and 51 km, respectively. In general, the spatial uncertainties are smaller for seismic sources located within the seismic array.

The landslide CSF models are inverted from using band-limited seismic data, and they best represent the macroscopic loading and unloading processes during landslide failures. Microscopic processes, such as the associated debris flow, may generate high frequency seismic radiation and are challenging to resolve with teleseismic records (Chmiel et al., 2021). The 1D velocity model used for Green's functions can capture the waveform shapes but cannot predict the surface wave arrival times accurately. To mitigate the 3D velocity influence, we apply empirical corrections before performing the inversion, which are obtained from cross-correlating the synthetic waveforms with the observations. We also examine the data influences in the CSF models by performing bootstrap resampling of the traces. The ensemble models from the bootstrap realizations are consistent with each other (Figure 4.3). In our method, we do not post-process the CSF models, and the onset of a landslide is determined as the first downward acceleration and the termination yields the forces reaching zero. Due to the limited frequency bandwidth used in the inversion, small oscillations are

present in the CSF models. However, they do not impact the main failure episodes very much (Figure 4.3). The waveform misfit is higher than typical values because we measure the ℓ_1 normalized residuals instead of the ℓ_2 normalized residuals. For comparison, our CSF model of the 2016 Lamplugh landslide is consistent with other published CSF models (Dufresne et al., 2019; Toney and Allstadt, 2021), and its failure process agrees with the surface structures resolved from field surveys Dufresne et al. (2019).

Optical images can directly validate the seismic detections. However, weather conditions may hinder timely verification of landslides in Alaska. For example, the first clear optical image of the 2017 Wrangell Mountains landslide from Sentinel-2 was taken on November 20, 2017 and the most recent cloud-free image before the landslide was taken on August 2, 2017. The three-month separation between the two acquisitions would hamper resolving the event occurrence time if we have only used optical images. In such cases, SAR imagery can provide a complementary verification for a better temporal resolution. For example, the two SAR images collected on September 20 and October 2, 2017 can provide a more timely assessment of the 2017 Wrangell Mountains landslide (12 days separation; Figure 4.9). The coherence changes in the SAR images sharply delineate a region with surface alteration (circled in Figure 4.9). The quasi-triangular geometry of the low coherence area suggests that it is most likely caused by a landslide (Mondini et al., 2021). In contrast, the SAR amplitude changes before and after the event are ambiguous at the landslide site, and the cause of the amplitude changes is less definitive without other independent geophysical evidence (Figure 4.10). The SAR images for the 2016 Lamplugh event

show the opposite sensitivities such that the differential radar amplitude works better as a proxy to identify landslides than the phase coherence (Mondini et al., 2019). The effectiveness of the phase decorrelation as a landslide marker is strongly affected by the mean coherence of the study area. If the coherence is low (e.g., due to vegetation or snow cover), a further reduction in coherence due to surface disturbance may not produce a clear anomaly. The effectiveness of the differential radar amplitude may depend on a distance between the repeat orbits (Manzo et al., 2012; Mastro et al., 2022). Larger perpendicular baselines may result in higher "background" values of the differential amplitude due to somewhat different lines of sight, which can reduce the signal-to-noise ratio for the amplitude changes caused by the landslide motion.

5.2 Mass Estimate of the 2017 Wrangell Mountains Landslide

The surface area of the 2017 Wrangell Mountains landslide is estimated as 1.6 km^2 using the Sentinel-2 images and 1.7 km^2 using the Sentinel-1 phase coherence anomaly (Figure 5.3). The satellite images suggest that the landslide has two branches, with the southern branch 8.4 times greater in area than the northern branch (Figure 5.3a). Therefore, we focus on the southern branch to estimate its mass. The observed surface alteration area likely consists of the source, sliding, and deposition areas. We assume that the mass is conserved and the landslide is a deep-seated event because of the coherent surface wavefield. In this case, if the displaced materials had a thickness around 50 m at the source region (Okuwaki et al., 2021; Xu et al., 2021) with an

area of 0.04 km^2 (200 m by 200 m, blue rectangle in Figure 5.3a), the mass estimate would be 5×10^9 kg assuming an average bedrock density of 2.5×10^3 kg/m^3 (Ridgway et al., 2007). By inspecting the Sentinel-2 image, the deposition area of the southern branch (green rectangle in Figure 5.3a) is estimated to be about 1.25 km^2, and the landslide mass would be 5×10^9 kg for an average thickness of 1.6 m at the deposition area. These mass estimates are based on the assumed landslide material thickness, and may be subject to large uncertainties. Better constraints on the landslide thickness can be obtained e.g. by differencing digital elevation models (Lin et al., 2006) provided such models are available with sufficient accuracy and resolution before and after the event. Following the empirical scaling relationship between the maximum centroid single force and the displaced mass in (Ekström and Stark, 2013), the southern branch of the Wrangell Mountains landslide may have moved a total mass of 7.8×10^9 kg, and the bootstrap ensemble models suggest a variation of the mass ranging from 7.5×10^9 kg to 8.6×10^9 kg within a 90% confidence interval.

We can further combine the parameters obtained from both the CSF model and space geodetic images for a better constrained mass estimate. The runout distance of the southern branch is estimated as about 700 m to 1500 m from the space geodetic observations, and the runout uncertainty reflects the possible range of the centroid location of the displaced mass. Given that the CSF model is the product of the displaced mass times the acceleration ($F = ma$), and the runout is the double integration of the horizontal acceleration (a_t) in the sliding direction, we can thus

estimate the displaced mass from

$$m = \frac{\int_{t_s}^{t_e} dt \int_{t_s}^{t_e} F_t dt}{L_t}, \tag{5.1}$$

where t_s and t_e are starting and terminating times of the sliding process, F_t is the horizontal force in the sliding direction, and $L_t = \int_{t_s}^{t_e} dt \int_{t_s}^{t_e} a_t dt$ is the runout distance. The horizontal force, F_t, can be obtained from the CSF model, and the runout distance can be measured from the space geodetic images. In practice, we forward calculate the trajectory using an assumed mass to identify the optimal value that best matches the runout distance resolved from the satellite imagery. Using the combined method, we obtain a mass estimate of $3.1 - 8.3 \times 10^9$ kg with the uncertainty range accounting for the runout distance uncertainties. In summary, the mass estimates from different methods are generally in agreement with each other. If we combine all the estimates, the displaced mass of the southern branch is likely in the range of $3.1 - 8.6 \times 10^9$ kg. The total mass of both branch is estimated in the range of $3.1 - 13.4 \times 10^9$ kg by evaluating the northern branch using the same set of techniques.

5.3 Failure Dynamics of the 2017 Wrangell Mountains Landslide

Satellite imagery from Sentinel-1 and Sentinel-2 (Figure 5.3) shows two separate deposits of the 2017 Wrangell Mountains landslide. However, it is unclear whether

the two piles of deposits were from the same landslide or from two separate landslides occurring within the acquisition intervals of satellite data. In the case of a single landslide scenario, the relations between the two subevents cannot be resolved using geodetic data alone. Complementary to the imagery, the seismic CSF model can offer insights into the failure trajectory (Figure C.1), but cannot resolve subevents for landslides because of its point source approximation.

Optical images from the Sentinel-2 satellite suggest that the source region of the 2017 Wrangell Mountains landslide is from a local mountain crest (the upper left region within the contour area in Figure 5.3a). The two deposits resulted from two distinct sliding trajectories with the northern branch sliding towards an azimuth of 116° and the southern branch sliding towards an azimuth of 175°. The CSF model indicates an initial sliding direction of 139° (Figure C.1), which is more consistent with the trajectory of the northern branch. Therefore, the northern subevent likely occurred first. The horizontal trajectory calculated from the CSF model can only match the topographic features at the northern branch up to 30 s, while the total failure process lasted for about 140 s (Figure C.1). The observations indicate that the southern branch may have occurred from 30 to 140 s, suggesting that the two branches were from one landslide. We denote the northern and southern branches as subevent 1 and 2, respectively.

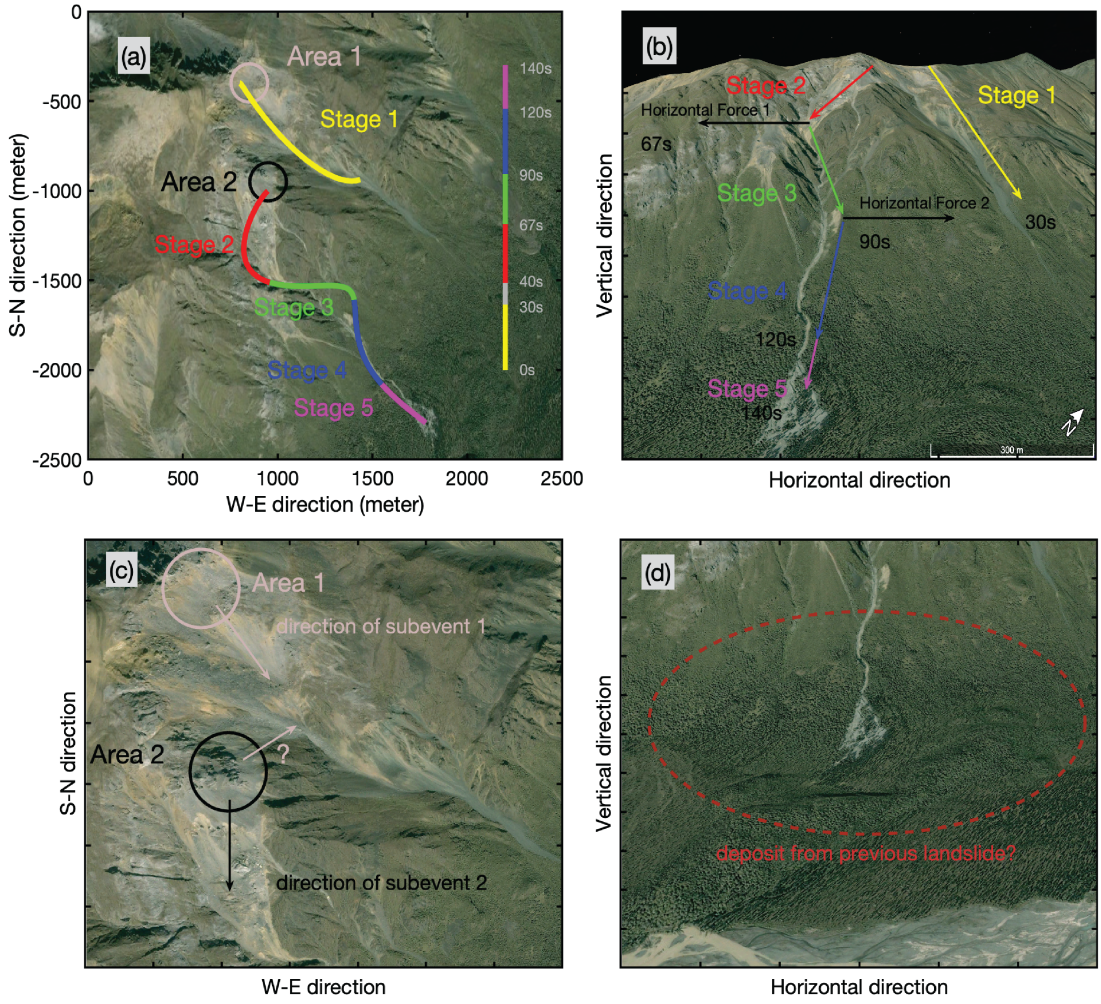

Figure 5.1: Inferred failure process of the 2017 Wrangell Mountains landslide. (a), Horizontal sliding trajectories of two subevents on a map-view satellite image. Colored lines represent five sliding stages with their occurrence times indicated in the colorbar. Overlapping time of the two subevents from 30–40 s are not interpreted. (b), Schematic sliding process on a vertical-view satellite image. (c), Zoom-in view of the source areas in (a). Area 1 and Area 2 are two possible initiation sites. Black arrow shows the sliding direction of Stage 2. Pink arrows show possible sliding directions of subevent 1. (d), Zoom-in view of the deposit area. Features in the red dash ellipse indicate a landslide occurred before 2004. Background images are from Google Earth^{TM} taken on August 4, 2004, provided by Maxar Technologies.

We therefore divide the CSF model into two parts to study the spatiotemporal evolution of the two subevents. The starting time of subevent 2 is determined by comparing the CSF horizontal trajectory to the topographic features (Appendix C and Figure C.2). The trajectory is the displacement integrated from the horizontal accelerations, which are obtained by dividing the mass estimates (1.5×10^9 kg for subevent , 3.5×10^9 kg for subevent 2) from the horizontal centroid single forces. The results show that the transition between the ending of subevent 1 and the initiation of subevent 2 most likely occurred at 40 s. There may have been a short overlap between the two subevents because the three-component centroid forces do not synchronize to zero at the same time, suggesting a possible concurrent ending and starting of the two subevents during 30–40 s.

While subevent 1 is relatively simple with one episode of sliding with a linear trajectory (Stage 1), subevent 2 likely had four sliding episodes lasting for about 100 s (Stages 2–5 in Figure 5.1a and 4.3d–f). Subevent 2 likely initiated from Area 2 in Figure 5.1c and slid toward a direction of 185° (Stage 2). The mobilized materials hit a mountain ridge with a southeast strike at 67 s and then turned towards a direction of 94°, sliding for another 23 s (Stage 3). Bounded in a valley, the subevent was forced to turn towards 164° at 90 s again and then moved along an incision valley from 90 to 120 s (Stage 4). When the failure material reached the bottom of the mountain at 120 s, the vertical centroid single force dropped to zero due to the low topographic relief, and the runout gradually lost its momentum (Stage 5). The Stage 5 sliding caused the material to spread out in a local basin with an approximate footprint of 1.25 km^2 (Figure 5.1a and 5.2). Visual inspections of the Sentinel-2 and

Google Earth satellite imagery (Figures 4.8c and 5.1a) suggest a possible overshoot of the failure material at the end of Stage 2. Some landslide material may have slid beyond the ridge around 50 s.

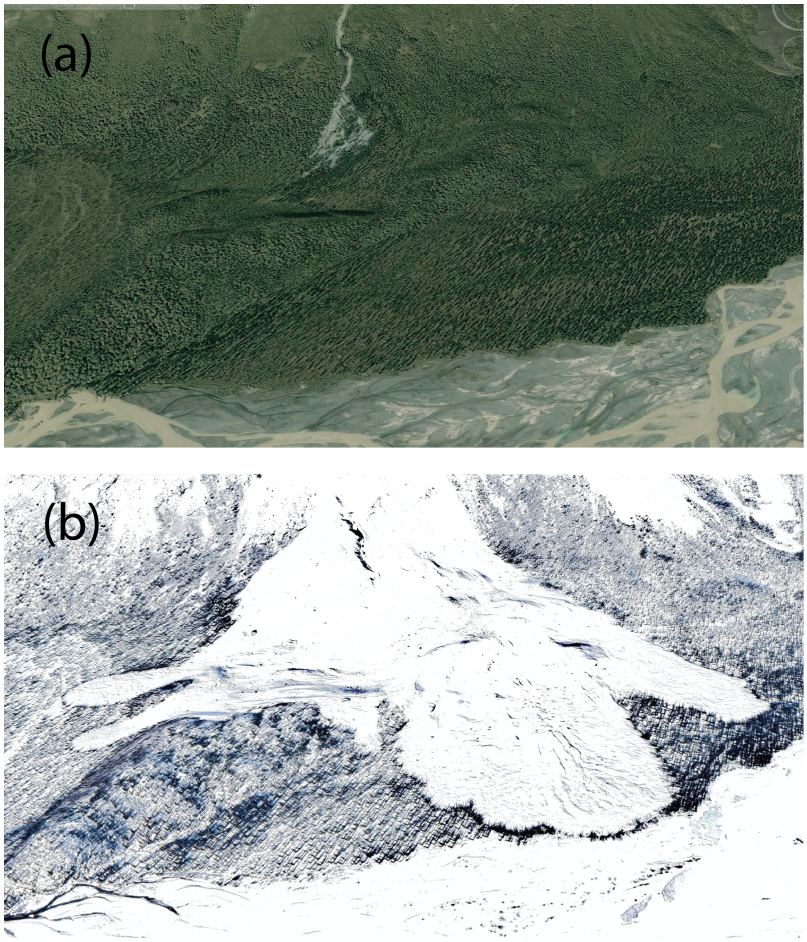

Figure 5.2: Zoom-in view of satellite images at the subevent 2 deposition area of the 2017 Wrangell Mountains landslide (a), Image acquired on August 4, 2004. (b), Image acquired on April 5, 2021. The satellite images are from Google Earth provided by Maxar Technologies. The area in (b) is covered by snow .

The peak sliding velocity of subevent 2 is about 39 m/s, assuming a failure mass of 3.5×10^9 kg. The sliding velocity is comparable to the 2015 Taan Fiord landslide

and the 2016 Lamplugh Glacier landslides. The failure processes of the two subevents inferred from the CSF model (horizontal displacements) match well with the trajectories identified from morphology features using satellite images (Figure 5.3). The vertical displacement is not used for inferences because it does not match the elevation changes (Figure D.1 and D.2). This is not surprising as CSF models of other Alaska landslides also have challenges in fitting the elevation changes (Toney et al., 2020; Toney and Allstadt, 2021). It is likely because the CSF model is obtained from band-limited seismic data and we used a 1D velocity model to compute the Green's functions. The unaccounted high-frequency data and the complex 3D velocity structure may have caused the poor resolution of the CSF model in vertical displacements. Further, noise in the seismic records likely contributed to the discrepancy as well.

Landslides may occur frequently in the region at the same spots. Figure 5.1d shows brown deposits near Stage 5, indicating a possible previous mass wasting event depositing at the same location. Further, the source areas (Areas 1 and 2) identified in Figure 5.1c were from an optical Maxar satellite image taken in 2004, which indicates previous landslides occurring before 2004. In conjunction with the 2017 landslide, the images indicate that the slope materials have been unstable for decades, and the material and topographic conditions may favor retrogressive landslides. The source areas are likely covered in snow in winter times (Figure 4.8b) and the snow would fully melt in summer times (Figure 4.8c). The rapid changes of surface hydraulic conditions would facilitate weathering and cause material disintegration, destabilizing the mountain slope at the source areas, and possibly leading to repeating landslides.

The current set of geophysical observations cannot conclusively determine the origin source region of subevent 1. The two subevents are separated by a mountain ridge, and subevent 1 could be from either Area 1 or 2 as highlighted in Figure 5.1c. The CSF model favors Area 1 as it does not indicate an initial acceleration towards the northeast direction, which would be expected if subevent 1 was from Area 2. However, as shown in Figure 5.1c, the 2004 satellite image suggests that materials from Area 2 may have slipped towards the trajectory of subevent 1 in previous landslides. The relics in Figure 5.1c suggest that subevent 2 came from the ridge denoted as Area 2. Therefore, both subevents of the 2017 Wrangell Mountains landslide may have originated from Area 2 as two pieces of one destabilized mass. Alternatively, subevent 1 may have originated from Area 1, and its failure destabilized mass in Area 2 and induced subevent 2. The sequential failure of the two subevents resolved in the CSF model (Figure 4.8) supports this scenario. Our observations suggest that failure processes of Alaska landslides can be highly complex and multiple subevents can trigger each other to cascade into greater landslides.

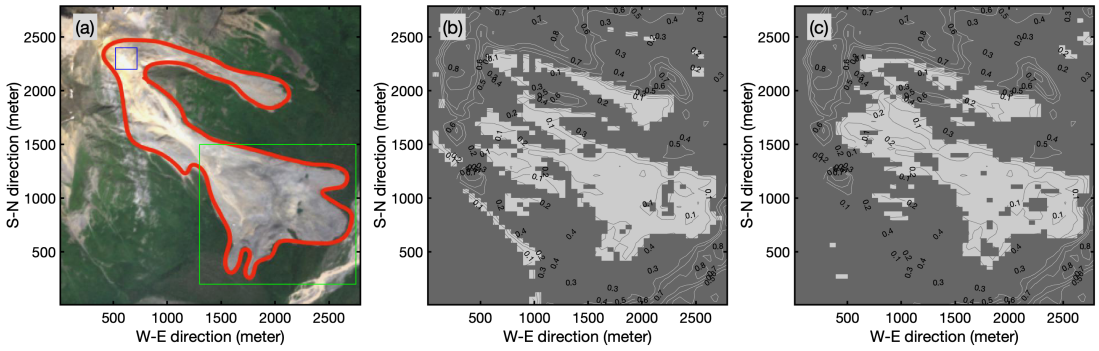

Figure 5.3: Area estimates of the 2017 Wrangell Mountains landslide. (a), Landslide area estimated using Sentinel-2 imagery. Red contour outlines the landslide. Thin blue box shows an assumed source area of subevent 2 and thin green box shows an assumed deposition region of subevent 2. (b) and (c), Coherence image of sub swath 2 and 3 with a mask threshold of 0.15. Masks of Sentinel-1 SAR coherence images obtained from two acquisitions on September 20 and October 2, 2017. Contours show the coherence values.

5.4 Outlook on Investigating Alaska Landslides

The two case studies presented above show that our integrated procedure is highly effective in identifying Alaska landslides and revealing their failure dynamics. In particular, the 2017 Wrangell Mountains landslide is one order of magnitude smaller than the Lamplugh Glacier landslide in mass, but had a more complex failure process. The 2017 Wrangell Mountains landslide is also much more complex than other recent landslides in Alaska (e.g., Gualtieri and Ekström, 2017; Toney et al., 2021). Our case study suggests that the failure processes of Alaska landslides are poorly known and emphasizes the necessity to systematically study landslides in the region. Our procedure has the potential to be applied to a large set of continuous records

to efficiently identify most, if not all, of the Alaska landslides above a certain detection threshold. Specifically, we can first use the AELUMA method to systematically detect and locate abnormal seismic sources and then use SAR and optical satellite data to quantitatively evaluate surface alternations in the seismic detection areas. The seismic detection method does not require phase-picking, an accurate velocity model, or knowing the source type. The SAR data products can be obtained from a number of providers, including e.g. routinely processed data products at the Alaska SAR Facility, and the optical images are freely provided by the European Space Agency. After confirming the events as landslides, our CSF modeling procedure is computationally efficient and designed to incorporate records from seismic stations within five degrees or even further from an event. The procedure requires an analyst to select an initial set of traces, but it can iteratively update the model based on all available data within the pre-selected distance range. Finally, we show that combining satellite imagery and seismically determined CSF models can yield a better understanding of the landslide dynamics.

Chapter 6

Conclusions

We developed an integrated procedure to use seismic and space geodetic observations to detect, locate and investigate the dynamic process of landslides in Alaska and other locations. We demonstrated that an array-based surface wave detector could be applied to the continuous waveform to detect landslides such as the 2016 Lamplugh Glacier landslides and 2017 Wrangell Mountains landslides.

We used geodetic data from Sentinel-1 and Sentinel-2 to confirm the detection from the seismology method. The seismic locations obtained from the seismology method are close to the landslide location obtained from geodetic data. Taking the 2016 Lamplugh Glacier landslide as a validation case, we showed that our seismically resolved location is within 3 km of the actual location ground truth-ed by the remote sensing data. The 2016 Lamplugh Glacier landslide can be clearly resolved in the radar amplitude changes obtained from Sentinel-1 SAR data. Applying the AELUMA detector to continuous seismic data in 2017, we identified a previously

unknown landslide in the Wrangell Mountains region. We use three Sentinel-2 acquisitions to confirm the location and the nature of the seismic detection. The color composite after the event shows the area of the landslide clearly. The coherence calculated using two SAR acquisitions from Sentinel-1 shows the landslide area has low coherence, and it can improve the confidence that the landslide in Sentinel-2 is associated with the detected seismic signal. The 2017 Wrangell Mountains landslide site is within 5 km of the seismically resolved location, demonstrating the robustness and accuracy of our procedure.

Further, We use regional seismic records to obtain a centroid single force model of the landslides. The CSF model for the 2016 Lamplugh Glacier landslide shows two downward acceleration stages, moving mostly in the north direction. The results agree with the previous studies. The CSF model for the 2017 Wrangell Mountains landslide is more complicated. It involves multiple accelerations and deceleration stages. But the inversion result is robust according to bootstrap inversion.

By combining seismic and space geodetic data, we confirm that the 2017 Wrangell Mountains landslide had two separate, sequential subevents, which involved five stages of sliding, and its dynamics were likely controlled by local terrain features. The results show that the smaller branch (subevent 1) happened first, and the larger branch(subevent 2) happened later. Subevent 1 is simple, with just one downward acceleration and deceleration process. Subevent 2 has four stages controlled by the topography features. This case suggests that small-scale landslides can still have a complicated dynamic process, and our procedure can effectively resolve such a process. Further, satellite images suggest the region may have landslides repeatedly

occurring at the same locations.

Through the case study here, it has been demonstrated that seismology and space geodetic methods can be combined to provide continuous monitoring of landslides in the Alaska region. The landslide mechanisms can be studied using the CSF model. The landslide dynamical process can be jointly constrained using the CSF model and satellite imagery such as Sentinel-1 and Sentinel-2. This approach can provide a very detailed dynamical process even for very small-scale landslides such as the Wrangell Mountains landslide. By combining seismic data and geodetic data, a complete long-term catalog was obtained using the procedure in this research. The catalog can also be used to understand climate change affects landslides in the Alaska region as well as other locations (Gariano and Guzzetti, 2016). Our results demonstrate that integrating multiple geophysical methods can illuminate complex landslide failure processes in Alaska and elsewhere.

The thesis, in full, has been submitted for publication of the material as it may appear in Journal of Geophysical Research-Earth Surface: Luo, X., Fan, W., and Fialko, Y., A joint seismic and space geodetic investigation of the 2016 Lamplugh Glacier and 2017 Wrangell Mountains (Alaska) landslides, submitted. I am the primary investigator and author of the paper.

Appendix A

Frequency Domain Inversion

We apply an iterative procedure using waveform similarity and waveform residual criteria (detailed in method) to determine the seismic record to include in the inversion.

Next, because the key parameters of landslides are important to estimate the impact and the mechanics, we can further use the centroid single force (Centroid Single Force) model to do that. The model characterizes the force exerted on the ground by the landslide. This is a first-order model that is decided by the landslide first-order movement as a whole. The model consists of three components force for North-South, West-East and vertical components. The recorded seismic signals from a landslide are decided by the centroid single force history is and the green function by the equation below:

$$u_n(\underline{x}, t) = G_{ni}(\underline{x}, t, \underline{\eta}, \tau) * F_i(\underline{\eta}, \tau) \tag{A.1}$$

where $\underline{x}$ denotes the seismometer location, η denotes the source location, u_n denotes the displacement at the seismometer at the n th direction, G_{ni} denotes the Green's function with a force source applied at the i th direction and received at n th direction, t and τ denote time, F_i denotes Centroid Single Force, i denotes the direction of the force (north-south, west-east and vertical). According to Green's function's time shift property, it can also be written as

$$u_n(\underline{x}, t) = G_{ni}(\underline{x}, t - \tau, \underline{\eta}, 0) * F_i(\underline{\eta}, \tau) \tag{A.2}$$

Now do a change of variable to make it clearer $t' = t - \tau$, which is time using the force source time as the origin. So the term $G_{ni}(\underline{x}, t - \tau, \underline{\eta}, 0) = G_{ni}(\underline{x}, t', \underline{\eta}, 0)$. $G_{ni}(\underline{x}, t', \underline{\eta}, 0)$ is the Green's function with a force source at origin time. The equation is then written as

$$u_n(\underline{x}, t) = G_{ni}(\underline{x}, t', \underline{\eta}, 0) * F_i(\underline{\eta}, \tau) \tag{A.3}$$

We solve this system in the frequency domain. Apply the Fourier transform to the equation. It is transformed to be a linear system as below (because it is convolution between function of t' and τ, those two variables are both transformed to ω):

$$\tilde{u}_n(\underline{x}, \omega) = \tilde{G}_{ni}(\underline{x}, \omega, \underline{\eta}, 0)\tilde{F}_i(\underline{\eta}, \omega) \tag{A.4}$$

It can be written in the matrix form as below by writing out the index n and i in terms of three directions 1,2 and 3,

$$U = GF \tag{A.5}$$

where

$$U = \begin{bmatrix} \tilde{u}_1(\underline{x}, \omega) \\ \tilde{u}_2(\underline{x}, \omega) \\ \tilde{u}_3(\underline{x}, \omega) \end{bmatrix} \tag{A.6}$$

$$G = \begin{bmatrix} \tilde{G}_{11}(\underline{x}, \omega, \underline{\eta}, 0) & \tilde{G}_{12}(\underline{x}, \omega, \underline{\eta}, 0) & \tilde{G}_{13}(\underline{x}, \omega, \underline{\eta}, 0) \\ \tilde{G}_{21}(\underline{x}, \omega, \underline{\eta}, 0) & \tilde{G}_{22}(\underline{x}, \omega, \underline{\eta}, 0) & \tilde{G}_{23}(\underline{x}, \omega, \underline{\eta}, 0) \\ \tilde{G}_{31}(\underline{x}, \omega, \underline{\eta}, 0) & \tilde{G}_{32}(\underline{x}, \omega, \underline{\eta}, 0) & \tilde{G}_{33}(\underline{x}, \omega, \underline{\eta}, 0) \end{bmatrix} \tag{A.7}$$

$$F = \begin{bmatrix} \tilde{F}_1(\underline{\eta}, \omega) \\ \tilde{F}_2(\underline{\eta}, \omega) \\ \tilde{F}_3(\underline{\eta}, \omega) \end{bmatrix} \tag{A.8}$$

This system can be solved using the least square inversion method. In practice, we include many good seismic records from many stations to include in the U matrix. we perform the Fast Fourier Transform (FFT) algorithm on the Green's function and the recorded seismograms. The nine components Green's function is obtained using the Instaseis method, which is obtained using axisymmetric spectral-element code AxiSEM with the anisotropy PREM model of up to 5s.Then for each frequency produced by FFT, we do the inversion in the frequency domain by using the least square inversion method. We use frequency from 0.0143Hz (70s) to 0.05Hz (20s) with 0.002Hz interval . Centroid single force models can be obtained in the frequency domain. Finally, we inverse transform the result into the time domain.

Appendix B

All Waveforms for CSF Inversion

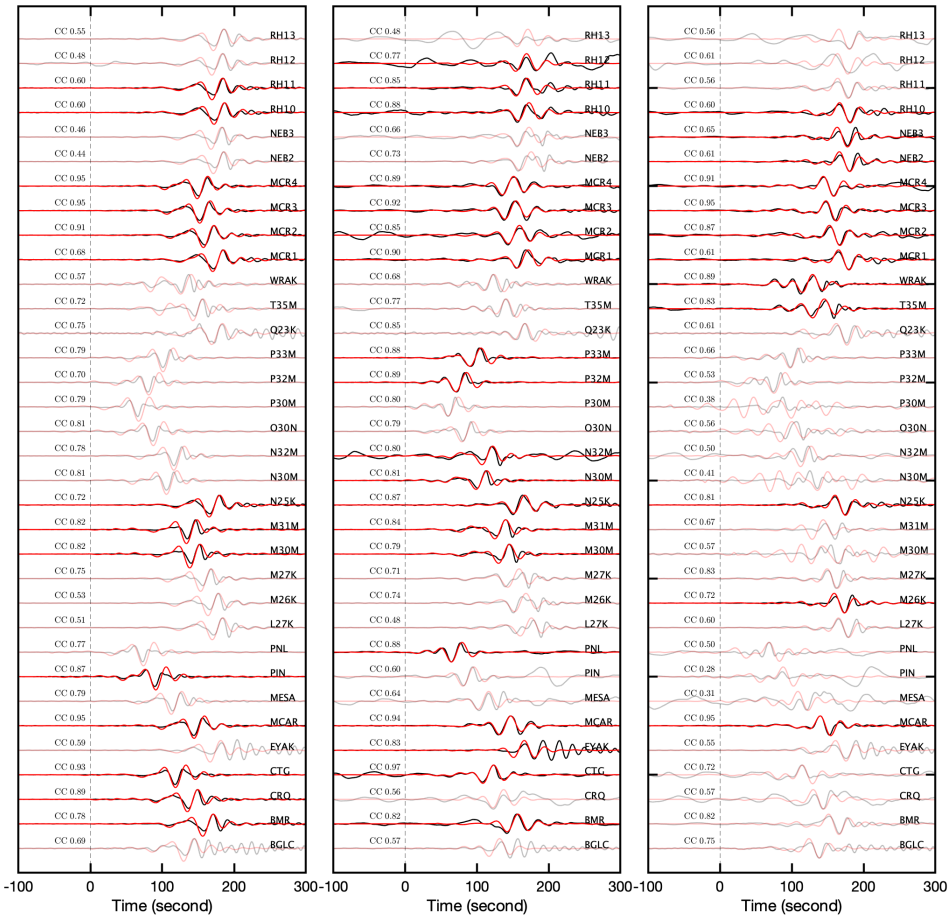

Figure B.1: All of the observed and synthetics seismograms for June 28, 2016 Lamplugh Glacier landslide within 5 degrees distance. Black lines are the observed seismograms. The red lines are synthetic seismograms. The traces with opaque color are traces not included in the final inversion.

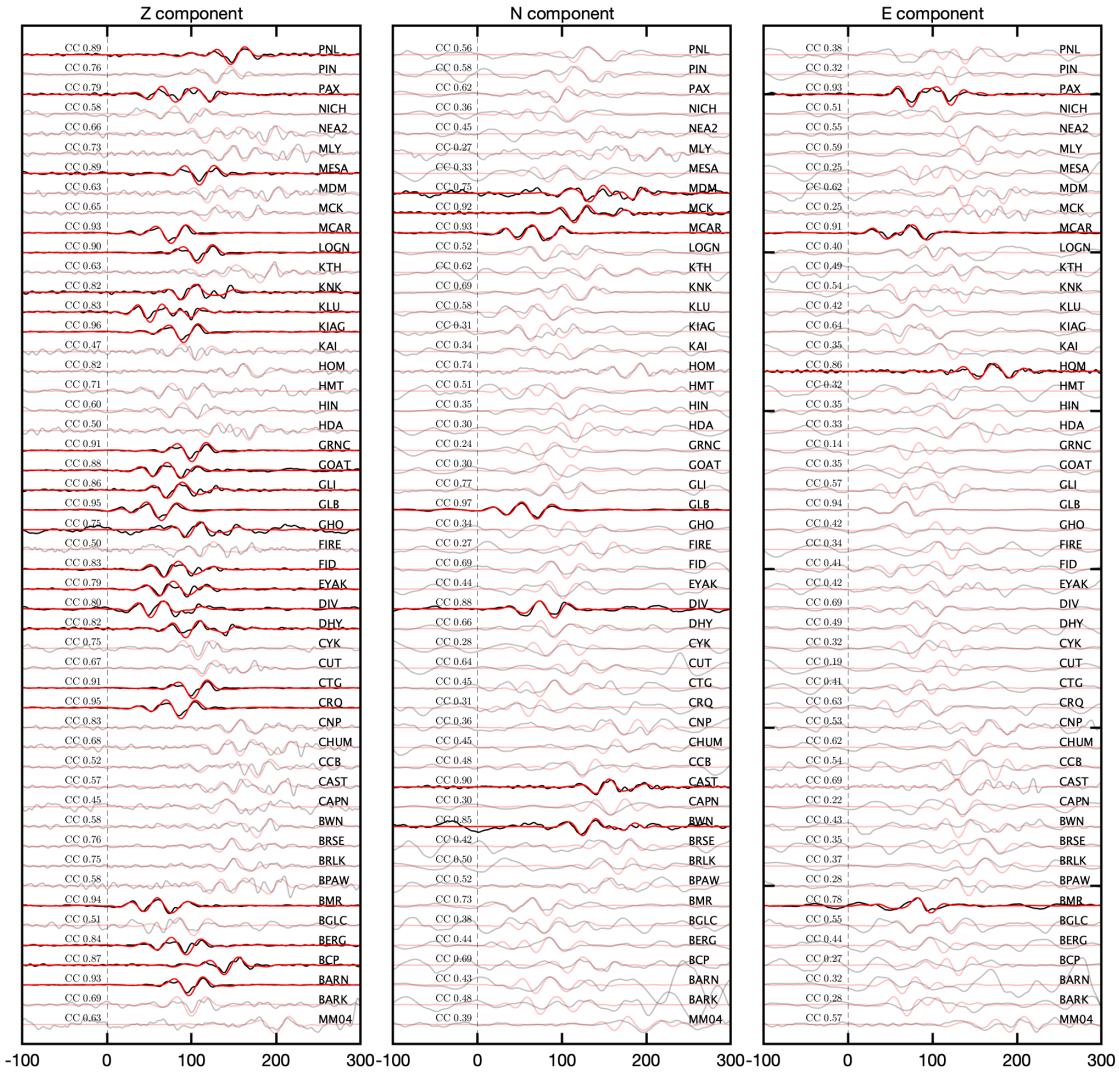

Figure B.2: All of the observed and synthetics seismograms for September 22, 2017 Wrangell Mountains landslide within 5 degrees distance (part 1). Black lines are the observed seismograms. The red lines are synthetic seismograms. The traces with opaque color are traces not included in the final inversion.

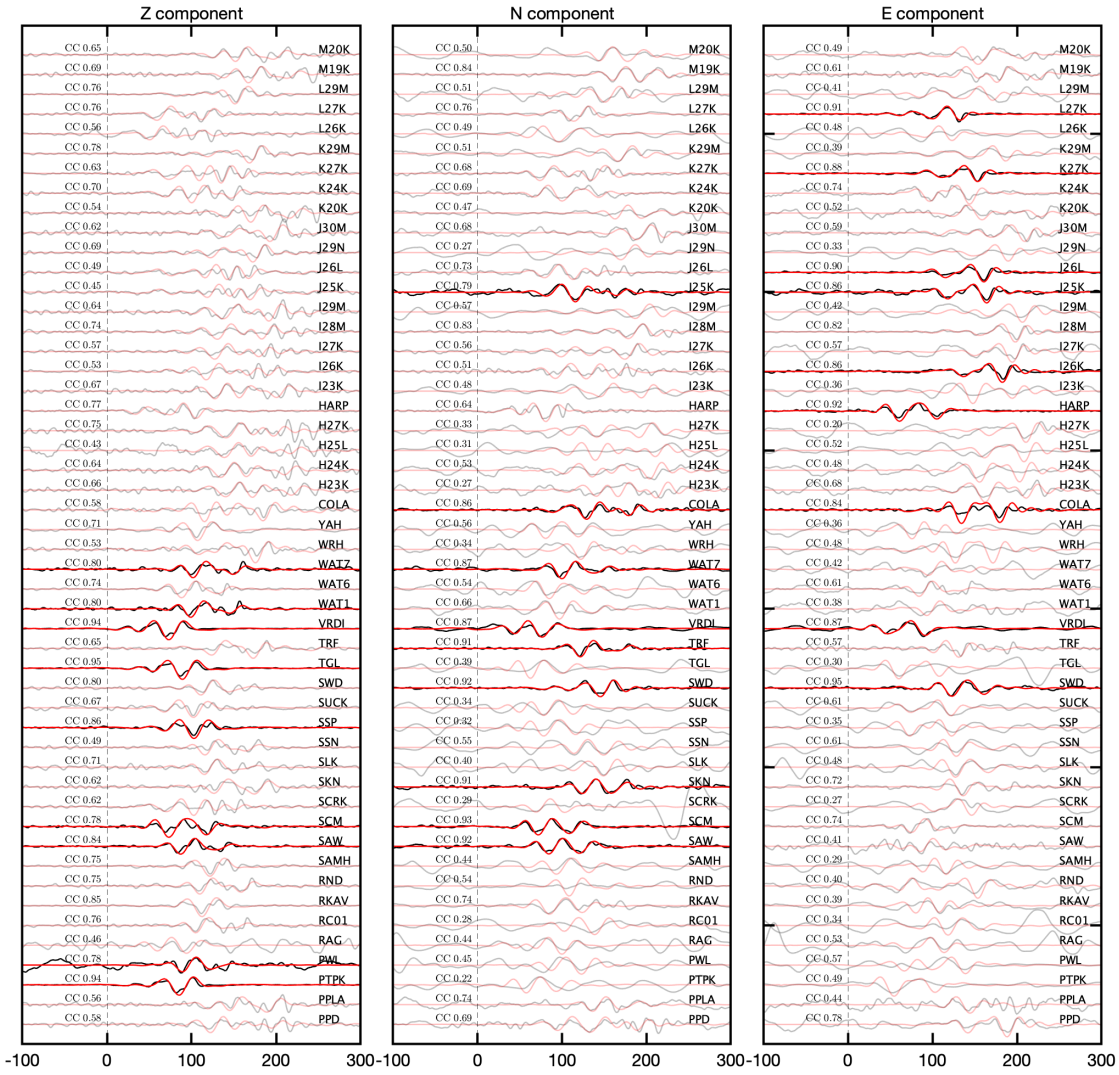

Figure B.3: All of the observed and synthetics seismograms for September 22, 2017 Wrangell Mountains landslide within 5 degrees distance (part 2). Black lines are the observed seismograms. The red lines are synthetic seismograms. The traces with opaque color are traces not included in the final inversion.

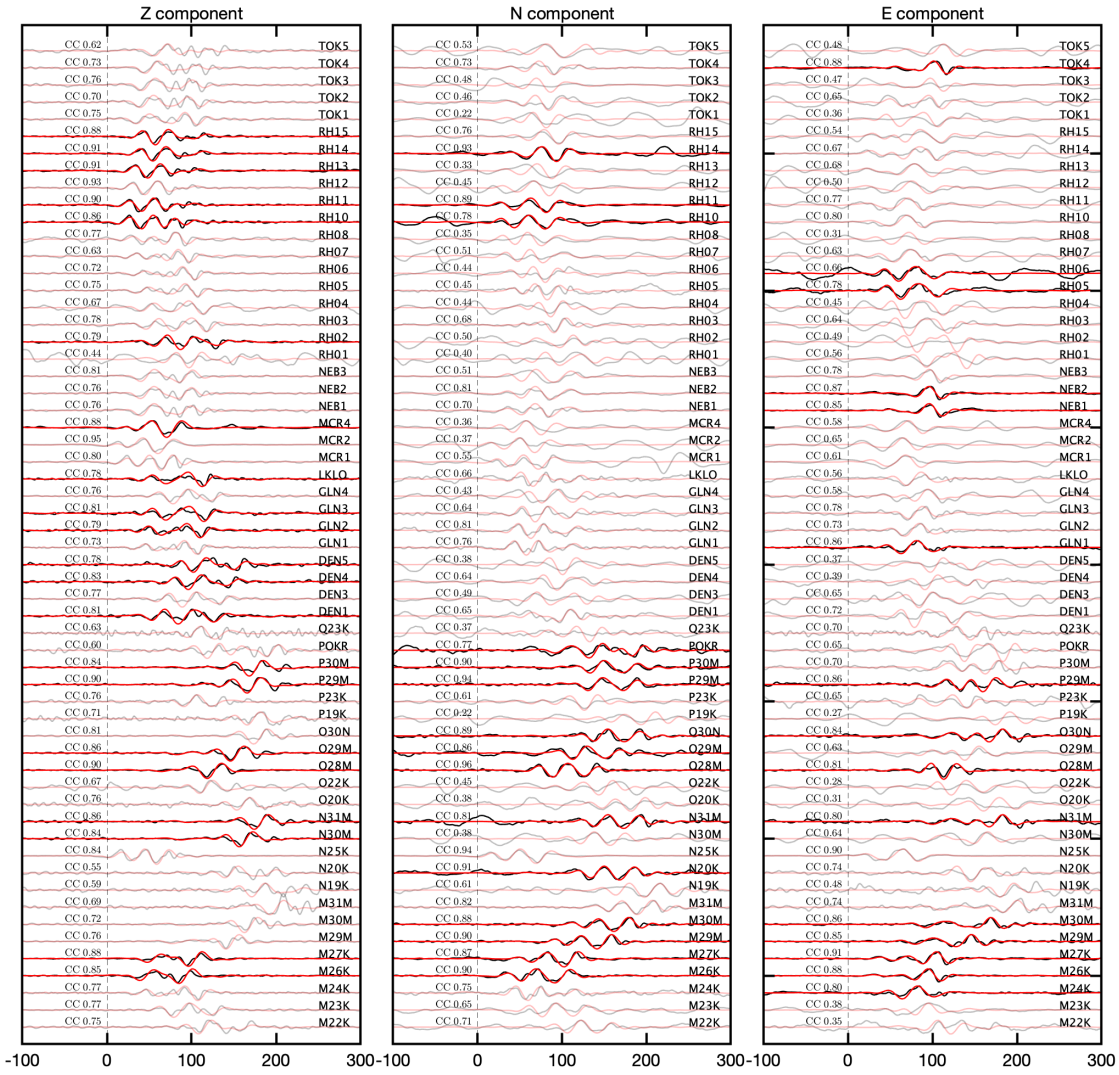

Figure B.4: All of the observed and synthetics seismograms for September 22, 2017 Wrangell Mountains landslide within 5 degrees distance (part 3). Black lines are the observed seismograms. The red lines are synthetic seismograms. The traces with opaque color are traces not included in the final inversion.

Appendix C

Decompose the CSF for Two Subevents

Topographic features can help constrain landslide sliding process Crowley et al. (2003); Gualtieri and Ekström (2018). The runout of subevent 1 observed in the satallite images matches the horizontal displacement integrated up to 30 s. Subevent 1 of the 2017 Wrangell Mountains landslide likely ended before 40 s because the trajectory of subevent 2 matches the topography precisely if its occurrence starts on 40 s (Figure C.2). The results suggest no significant amount of forces produced by subevent 1 after 40 s. In Figure C.1, the southward trajectory cannot be explained by the topography of the incision valley near subevent 1. However, such a direction can be explained by the topography near subevent 2. The two subevents may have overlapped because the three-component centroid signal forces do not synchronize to zero in between 30 to 40 s.

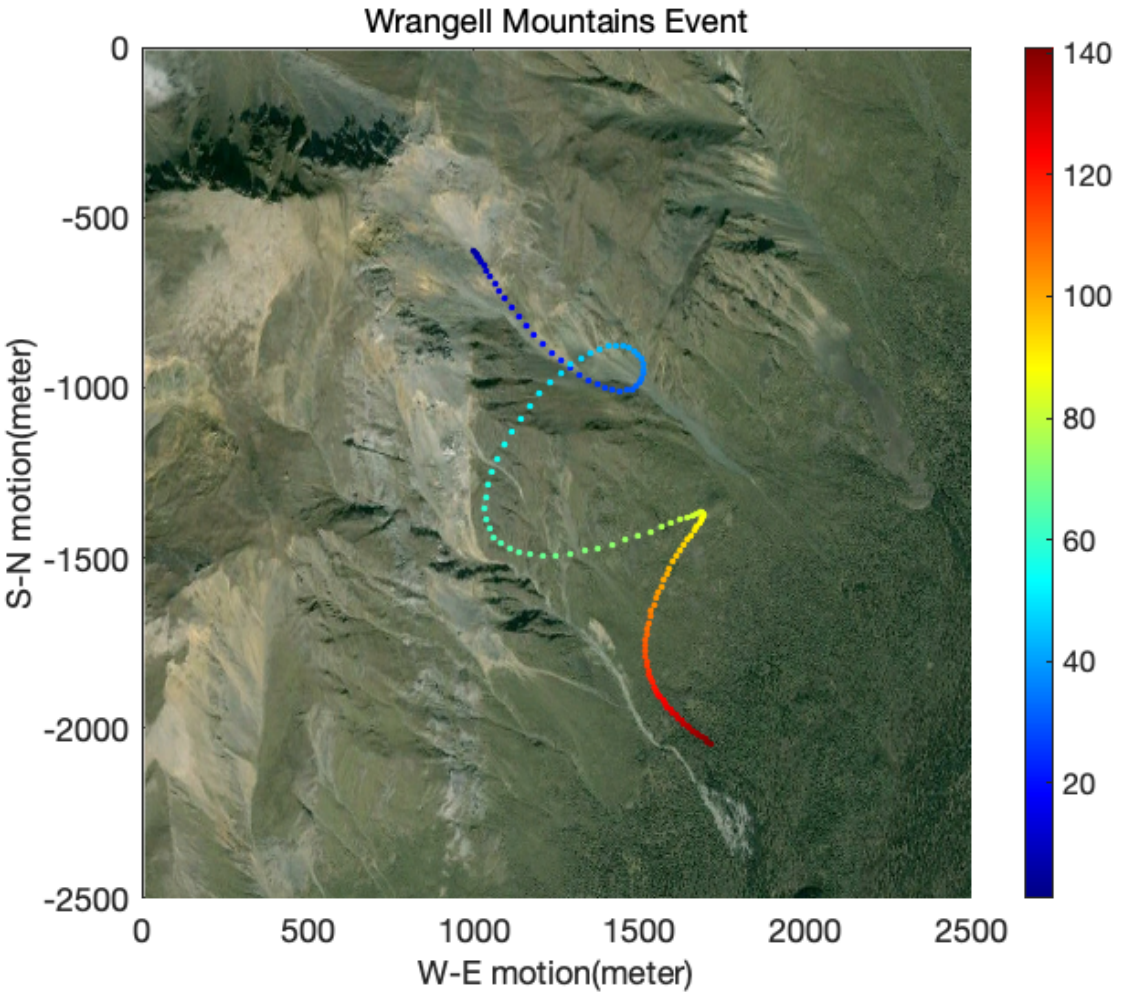

Figure C.1: Horizontal trajectory determined from integrating the accelerations, assuming a mass of 2×10^9 kg. Color dots represent the time since the origin time. Background satellite image is from Google Earth provided by Maxar Technologies.

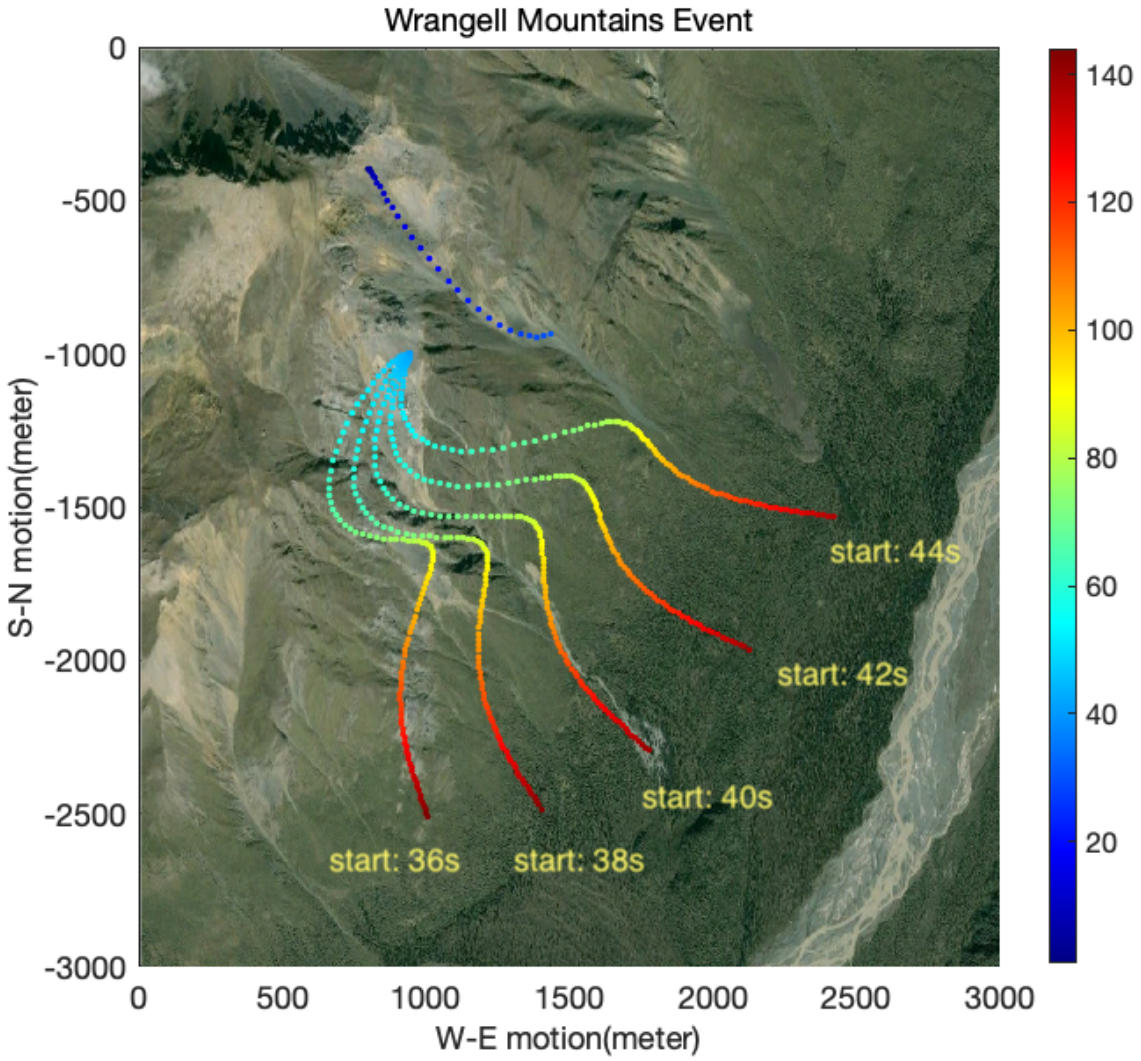

Figure C.2: Horizontal trajectory determined from integrating the accelerations, assuming a mass of 1.5×10^9 kg for subevent 1 and a mass of 3.5×10^9 kg for subevent 2. Color dots represent the time since the origin time. Background satellite image is from Google Earth provided by Maxar Technologies.

Appendix D

Vertical Displacement Profile for Two Subevents

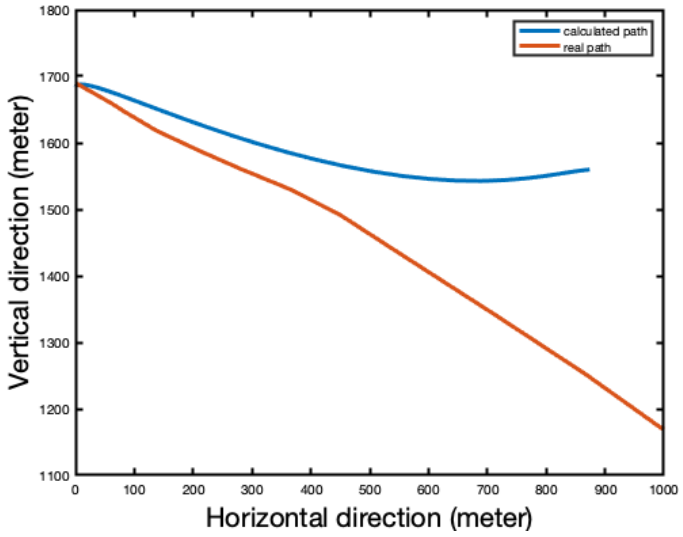

Figure D.1: Vertical displacement of subevent 1 of the Wrangell Mountains landslide. Blue line is the vertical displacement integrated from the vertical acceleration. Red line is the measured elevation.

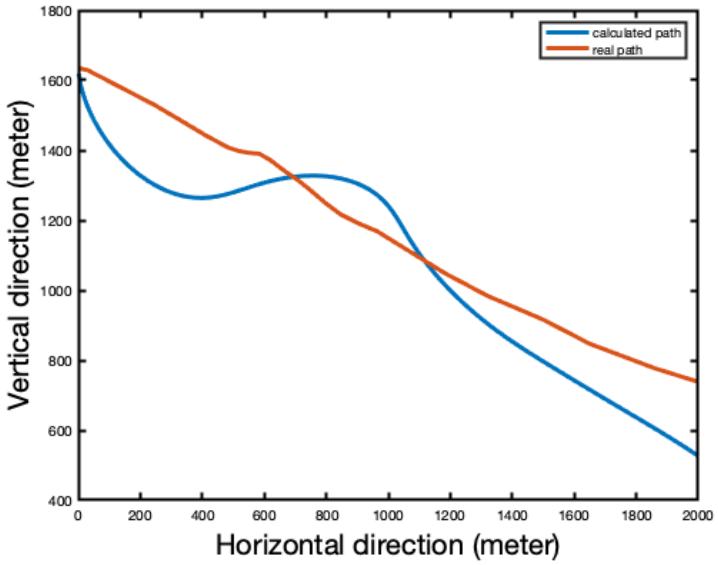

Figure D.2: Vertical displacement of subevent 2 of the Wrangell Mountains landslide. Blue line is the vertical displacement integrated from the vertical acceleration. Red line is the measured elevation variation.

Appendix E

Calculated Trajectory

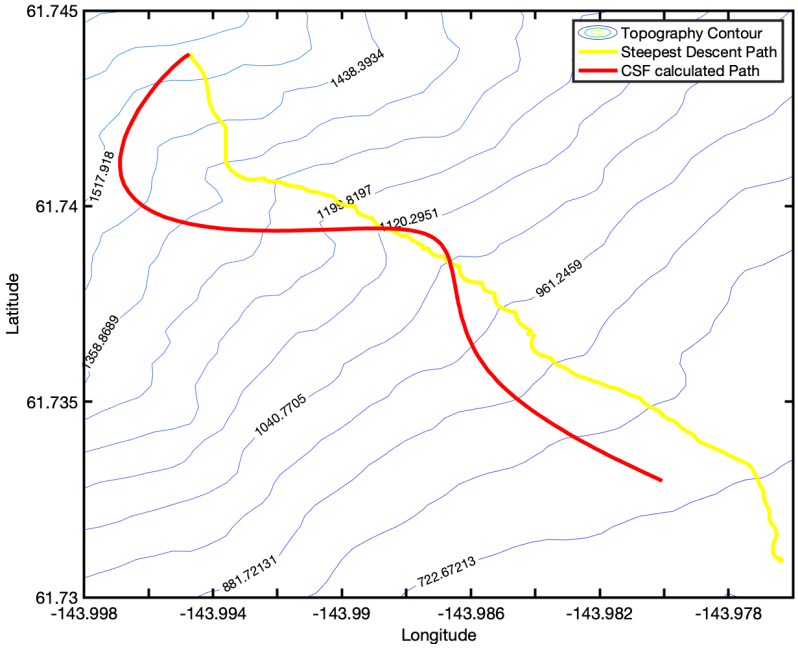

Figure E.1: Horizontal trajectory of subevent 2 determined from using the CSF model and the steepest descent path according to the ALOS AD3D30 digital elevation model.

Appendix F

Mass Estimations for Two Subevents

Table F.1: Maximum centroid single forces and mass estimation following (Ekström and Stark, 2013) for the 2017 Wrangell Mountains landslide

	Subevent 1	Subevent 2	Total
Maximum force	0.864×10^{10} N	1.448×10^{10} N	
Mass estimate	4.66×10^{9} kg	7.82×10^{9} kg	12.48×10^{9} kg
90% confidence interval, maximum force	$0.831/0.891 \times 10^{10}$ N	$1.392/1.583 \times 10^{10}$ N	
90% confidence interval, mass estimate	$4.49/4.81 \times 10^{9}$ kg	$7.52/8.55 \times 10^{9}$ kg	$12.01/13.36 \times 10^{9}$ kg

Table F.2: Mass estimate based on geodetic and seismc observations

	Subevent 1	Subevent 2	Total
Mass runout distance	600 m	1000 m	
Mass estimate	1.5×10^9 kg	3.5×10^9 kg	5.0×10^9 kg
Mass runout range	$300 - 1500$ m	$700 - 1500$ m	
Mass estimate range	$0.6/3 \times 10^9$ kg	$2.5/5.3 \times 10^9$ kg	$3.1/8.3 \times 10^9$ kg

Table F.3: Mass estimate based on area and thickness

	Subevent 1	Subevent 2	Total
Total area	0.23 km^2	1.47 km^2	1.70 km^2
Source area	0.01 km^2	0.04 km^2	0.05 km^2
Passage area	0.05 km^2	0.18 km^2	0.23 km^2
Deposition area	0.17 km^2	1.25 km^2	1.43 km^2
Assumed source thickness	50 m	50 m	
Assumed deposition thickness	1.6 m	2.9 m	
Assumed density	2.5×10^3 kg/m^3	2.5×10^3 kg/m^3	
Mass estimate	1.25×10^9 kg	5.01×10^9 kg	6.25×10^9 kg

References

Allstadt, K. (2013). Extracting source characteristics and dynamics of the august 2010 mount meager landslide from broadband seismograms. *Journal of Geophysical Research: Earth Surface*, 118(3):1472–1490.

Bahavar, M., Allstadt, K. E., Van Fossen, M., Malone, S. D., and Trabant, C. (2019). Exotic seismic events catalog (esec) data product. *Seismological Research Letters*, 90(3):1355–1363.

Bardet, J.-P., Synolakis, C. E., Davies, H. L., Imamura, F., and Okal, E. A. (2003). Landslide tsunamis: Recent findings and research directions. *Landslide tsunamis: recent findings and research directions*, pages 1793–1809.

Benda, L. and Dunne, T. (1997). Stochastic forcing of sediment supply to channel networks from landsliding and debris flow. *Water Resources Research*, 33(12):2849–2863.

Bessette-Kirton, E. K., Coe, J. A., and Zhou, W. (2018). Using stereo satellite imagery to account for ablation, entrainment, and compaction in volume calculations for rock avalanches on glaciers: Application to the 2016 lamplugh rock avalanche in glacier bay national park, alaska. *Journal of Geophysical Research: Earth Surface*, 123(4):622–641.

Brodsky, E. E., Gordeev, E., and Kanamori, H. (2003). Landslide basal friction as measured by seismic waves. *Geophysical Research Letters*, 30(24).

Chmiel, M., Walter, F., Wenner, M., Zhang, Z., McArdell, B. W., and Hibert, C. (2021). Machine learning improves debris flow warning. *Geophysical Research Letters*, 48(3):e2020GL090874.

Coe, J. A., Bessette-Kirton, E. K., and Geertsema, M. (2018). Increasing rock-

avalanche size and mobility in glacier bay national park and preserve, alaska detected from 1984 to 2016 landsat imagery. *Landslides*, 15(3):393–407.

Colesanti, C. and Wasowski, J. (2006). Investigating landslides with space-borne synthetic aperture radar (sar) interferometry. *Engineering geology*, 88(3-4):173–199.

Crowley, J., Hubbard, B., and Mars, J. (2003). Analysis of potential debris flow source areas on mount shasta, california, by using airborne and satellite remote sensing data. *Remote Sensing of Environment*, 87(2-3):345–358.

Dammeier, F., Moore, J. R., Hammer, C., Haslinger, F., and Loew, S. (2016). Automatic detection of alpine rockslides in continuous seismic data using hidden markov models. *Journal of Geophysical Research: Earth Surface*, 121(2):351–371.

Dammeier, F., Moore, J. R., Haslinger, F., and Loew, S. (2011). Characterization of alpine rockslides using statistical analysis of seismic signals. *Journal of Geophysical Research: Earth Surface*, 116(F4).

de Groot-Hedlin, C. D. and Hedlin, M. A. (2015). A method for detecting and locating geophysical events using groups of arrays. *Geophysical Journal International*, 203(2):960–971.

de Groot-Hedlin, C. D. and Hedlin, M. A. (2018). A new automated approach to detecting and locating seismic events using data from a large network. *Bulletin of the Seismological Society of America*.

Delbridge, B. G., Bürgmann, R., Fielding, E., Hensley, S., and Schulz, W. H. (2016). Three-dimensional surface deformation derived from airborne interferometric uavsar: Application to the slumgullion landslide. *Journal of geophysical research: solid earth*, 121(5):3951–3977.

Deparis, J., Jongmans, D., Cotton, F., Baillet, L., Thouvenot, F., and Hantz, D. (2008). Analysis of rock-fall and rock-fall avalanche seismograms in the french alps. *Bulletin of the Seismological Society of America*, 98(4):1781–1796.

Doi, I. and Maeda, T. (2020). Landslide characteristics revealed by high-frequency seismic waves from the 2017 landslide in central japan. *Seismological Society of America*, 91(5):2719–2729.

Dufresne, A., Geertsema, M., Shugar, D., Koppes, M., Higman, B., Haeussler, P., Stark, C., Venditti, J., Bonno, D., Larsen, C., et al. (2018). Sedimentology and geomorphology of a large tsunamigenic landslide, taan fiord, alaska. *Sedimentary Geology*, 364:302–318.

Dufresne, A., Wolken, G., Hibert, C., Bessette-Kirton, E., Coe, J. A., Geertsema, M., and Ekström, G. (2019). The 2016 lamplugh rock avalanche, alaska: deposit structures and emplacement dynamics. *Landslides*, 16(12):2301–2319.

Ekstrom, G. (2006). Global detection and location of seismic sources by using surface waves. *Bulletin of the Seismological Society of America*, 96(4A):1201.

Ekström, G., Nettles, M., and Dziewoński, A. (2012). The global cmt project 2004–2010: Centroid-moment tensors for 13,017 earthquakes. *Physics of the Earth and Planetary Interiors*, 200:1–9.

Ekström, G. and Stark, C. P. (2013). Simple scaling of catastrophic landslide dynamics. *Science*, 339(6126):1416–1419.

Fan, W., de Groot Hedlin, C. D., Hedlin, M. A. H., and Ma, Z. (2018). Using surface waves recorded by a large mesh of three-element arrays to detect and locate disparate seismic sources. *Geophysical Journal International*, 215(2):942–958.

Fan, W., McGuire, J. J., de Groot-Hedlin, C. D., Hedlin, M. A., Coats, S., and Fiedler, J. W. (2019). Stormquakes. *Geophysical Research Letters*.

Fan, W., McGuire, J. J., and Shearer, P. M. (2020). Abundant spontaneous and dynamically triggered submarine landslides in the gulf of mexico. *Geophysical Research Letters*, 47(12):e2020GL087213.

Fan, W., Shearer, P. M., and Gerstoft, P. (2014). Kinematic earthquake rupture inversion in the frequency domain. *Geophysical Journal International*, 199(2):1138–1160.

Fan, X., Xu, Q., Scaringi, G., Dai, L., Li, W., Dong, X., Zhu, X., Pei, X., Dai, K., and Havenith, H.-B. (2017). Failure mechanism and kinematics of the deadly june 24th 2017 xinmo landslide, maoxian, sichuan, china. *Landslides*, 14(6):2129–2146.

Feng, L. and Ritzwoller, M. H. (2019). A 3-d shear velocity model of the crust and uppermost mantle beneath alaska including apparent radial anisotropy. *Journal*

of Geophysical Research: Solid Earth, 124(10):10468–10497.

Froude, M. J. and Petley, D. N. (2018). Global fatal landslide occurrence from 2004 to 2016. *Natural Hazards and Earth System Sciences*, 18(8):2161–2181.

Fruneau, B., Achache, J., and Delacourt, C. (1996). Observation and modelling of the saint-etienne-de-tinée landslide using sar interferometry. *Tectonophysics*, 265(3-4):181–190.

Fukao, Y. (1995). Single-force representation of earthquakes due to landslides or the collapse of caverns. *Geophysical Journal International*, 122(1):243–248.

Gariano, S. L. and Guzzetti, F. (2016). Landslides in a changing climate. *Earth-Science Reviews*, 162:227–252.

Gomberg, J., Bodin, P., Savage, W., and Jackson, M. E. (1995). Landslide faults and tectonic faults, analogs?: The slumgullion earthflow, colorado. *Geology*, 23(1):41–44.

Gomi, T., Sidle, R. C., and Richardson, J. S. (2002). Understanding processes and downstream linkages of headwater systems: headwaters differ from downstream reaches by their close coupling to hillslope processes, more temporal and spatial variation, and their need for different means of protection from land use. *BioScience*, 52(10):905–916.

Grant, M. and Boyd, S. (2008). Graph implementations for nonsmooth convex programs. In Blondel, V., Boyd, S., and Kimura, H., editors, *Recent Advances in Learning and Control*, Lecture Notes in Control and Information Sciences, pages 95–110. Springer-Verlag Limited.

Grant, M. and Boyd, S. (2014). CVX: Matlab software for disciplined convex programming, version 2.1.

Gualtieri, L. and Ekström, G. (2017). Seismic reconstruction of the 2012 palisades rockfall using the analytical solution to lamb's problem. *Bulletin of the Seismological Society of America*, 107(1):63–71.

Gualtieri, L. and Ekström, G. (2018). Broad-band seismic analysis and modeling of the 2015 taan fjord, alaska landslide using instaseis. *Geophysical Journal International*, 213(3):1912–1923.

Guthrie, R., Friele, P., Allstadt, K., Roberts, N., Evans, S., Delaney, K., Roche, D., Clague, J., and Jakob, M. (2012). The 6 august 2010 mount meager rock slide-debris flow, coast mountains, british columbia: characteristics, dynamics, and implications for hazard and risk assessment. *Natural Hazards and Earth System Sciences*, 12(5):1277–1294.

Hibert, C., Mangeney, A., Grandjean, G., and Shapiro, N. (2011). Slope instabilities in dolomieu crater, réunion island: From seismic signals to rockfall characteristics. *Journal of Geophysical Research: Earth Surface*, 116(F4).

Hibert, C., Stark, C., and Ekström, G. (2015). Dynamics of the oso-steelhead landslide from broadband seismic analysis. *Natural Hazards and Earth System Sciences*, 15(6):1265–1273.

Higman, B., Shugar, D. H., Stark, C. P., Ekström, G., Koppes, M. N., Lynett, P., Dufresne, A., Haeussler, P. J., Geertsema, M., Gulick, S., et al. (2018). The 2015 landslide and tsunami in taan fiord, alaska. *Scientific Reports*, 8(1):1–12.

Hu, X., Bürgmann, R., Lu, Z., Handwerger, A. L., Wang, T., and Miao, R. (2019). Mobility, thickness, and hydraulic diffusivity of the slow-moving monroe landslide in california revealed by l-band satellite radar interferometry. *Journal of Geophysical Research: Solid Earth*, 124(7):7504–7518.

Huang, C.-J., Yin, H.-Y., Chen, C.-Y., Yeh, C.-H., and Wang, C.-L. (2007). Ground vibrations produced by rock motions and debris flows. *Journal of Geophysical Research: Earth Surface*, 112(F2).

Imaizumi, F. and Sidle, R. C. (2007). Linkage of sediment supply and transport processes in miyagawa dam catchment, japan. *Journal of Geophysical Research: Earth Surface*, 112(F3).

Intrieri, E., Raspini, F., Fumagalli, A., Lu, P., Del Conte, S., Farina, P., Allievi, J., Ferretti, A., and Casagli, N. (2018). The maoxian landslide as seen from space: detecting precursors of failure with sentinel-1 data. *Landslides*, 15(1):123–133.

Iverson, R. M., Reid, M., Iverson, N. R., LaHusen, R., Logan, M., Mann, J., and Brien, D. (2000). Acute sensitivity of landslide rates to initial soil porosity. *science*, 290(5491):513–516.

Jiang, C., Schmandt, B., Ward, K. M., Lin, F.-C., and Worthington, L. L. (2018).

Upper mantle seismic structure of alaska from rayleigh and s wave tomography. *Geophysical Research Letters*, 45(19):10–350.

Kanamori, H. and Given, J. W. (1982). Analysis of long-period seismic waves excited by the may 18, 1980, eruption of mount st. helens—a terrestrial monopole? *Journal of Geophysical Research: Solid Earth*, 87(B7):5422–5432.

Kawakatsu, H. (1989a). Centroid single force inversion of seismic waves generated by landslides. *Journal of Geophysical Research: Solid Earth*, 94(B9):12363–12374.

Kawakatsu, H. (1989b). Centroid single force inversion of seismic waves generated by landslides. *Journal of Geophysical Research: Solid Earth*, 94(B9):12363–12374.

Kirschbaum, D., Stanley, T., and Zhou, Y. (2015). Spatial and temporal analysis of a global landslide catalog. *Geomorphology*, 249:4–15.

Korup, O. (2005). Geomorphic imprint of landslides on alpine river systems, southwest new zealand. *Earth Surface Processes and Landforms*, 30(7):783–800.

Korup, O., Clague, J. J., Hermanns, R. L., Hewitt, K., Strom, A. L., and Weidinger, J. T. (2007). Giant landslides, topography, and erosion. *Earth and Planetary Science Letters*, 261(3-4):578–589.

Lacroix, P., Bièvre, G., Pathier, E., Kniess, U., and Jongmans, D. (2018). Use of sentinel-2 images for the detection of precursory motions before landslide failures. *Remote Sensing of Environment*, 215:507–516.

Lai, V. H., Tsai, V. C., Lamb, M. P., Ulizio, T. P., and Beer, A. R. (2018). The seismic signature of debris flows: Flow mechanics and early warning at montecito, california. *Geophysical Research Letters*, 45(11):5528–5535.

Li, W., Chen, Y., Liu, F., Yang, H., Liu, J., and Fu, B. (2019). Chain-style landslide hazardous process: Constraints from seismic signals analysis of the 2017 xinmo landslide, sw china. *Journal of Geophysical Research: Solid Earth*, 124(2):2025–2037.

Lin, G., Shearer, P. M., and Fialko, Y. (2006). Obtaining absolute locations for quarry seismicity using remote sensing data. *Bull. Seismol. Soc. Am.*, 96:722–728.

Manconi, A., Picozzi, M., Coviello, V., De Santis, F., and Elia, L. (2016). Real-time

detection, location, and characterization of rockslides using broadband regional seismic networks. *Geophysical Research Letters*, 43(13):6960–6967.

Manzo, M., Fialko, Y., Casu, F., Pepe, A., and Lanari, R. (2012). A quantitative assessment of DInSAR measurements of interseismic deformation: the Southern San Andreas Fault case study. *Pure Appl. Geoph.*, 168:195–210.

Mastro, P., Masiello, G., Serio, C., and Pepe, A. (2022). Change detection techniques with synthetic aperture radar images: Experiments with random forests and sentinel-1 observations. *Remote Sensing*, 14(14):3323.

Milillo, P., Fielding, E. J., Shulz, W. H., Delbridge, B., and Burgmann, R. (2014). Cosmo-skymed spotlight interferometry over rural areas: The slumgullion landslide in colorado, usa. *IEEE Journal of Selected Topics in Applied Earth Observations and Remote Sensing*, 7(7):2919–2926.

Mondini, A. C., Guzzetti, F., Chang, K.-T., Monserrat, O., Martha, T. R., and Manconi, A. (2021). Landslide failures detection and mapping using synthetic aperture radar: Past, present and future. *Earth-Science Reviews*, page 103574.

Mondini, A. C., Santangelo, M., Rocchetti, M., Rossetto, E., Manconi, A., and Monserrat, O. (2019). Sentinel-1 sar amplitude imagery for rapid landslide detection. *Remote sensing*, 11(7):760.

Moretti, L., Mangeney, A., Capdeville, Y., Stutzmann, E., Huggel, C., Schneider, D., and Bouchut, F. (2012). Numerical modeling of the mount steller landslide flow history and of the generated long period seismic waves. *Geophysical Research Letters*, 39(16).

Nayak, A., Eberhart-Phillips, D., Ruppert, N. A., Fang, H., Moore, M. M., Tape, C., Christensen, D. H., Abers, G. A., and Thurber, C. H. (2020). 3d seismic velocity models for alaska from joint tomographic inversion of body-wave and surface-wave data. *Seismological Research Letters*, 91(6):3106–3119.

Nissen-Meyer, T., Driel, M. v., Stähler, S., Hosseini, K., Hempel, S., Auer, L., Colombi, A., and Fournier, A. (2014). Axisem: broadband 3-d seismic wavefields in axisymmetric media. *Solid Earth*, (1):425–445.

Norris, R. D. (1994). Seismicity of rockfalls and avalanches at three cascade range volcanoes: Implications for seismic detection of hazardous mass movements. *Bul-*

letin of the Seismological Society of America, 84(6):1925–1939.

Okuwaki, R., Fan, W., Yamada, M., Osawa, H., and Wright, T. J. (2021). Identifying landslides from continuous seismic surface waves: a case study of multiple small-scale landslides triggered by typhoon talas, 2011. *Geophysical Journal International*, 226(2):729–741.

Petley, D. (2012). Global patterns of loss of life from landslides. *Geology*, 40(10):927–930.

Poli, P. (2017). Creep and slip: Seismic precursors to the nuugaatsiaq landslide (greenland). *Geophysical Research Letters*, 44(17):8832–8836.

Qu, F., Qiu, H., Sun, H., and Tang, M. (2021). Post-failure landslide change detection and analysis using optical satellite sentinel-2 images. *Landslides*, 18(1):447–455.

Rees, W. G. (2013). *Physical principles of remote sensing*. Cambridge university press.

Ridgway, K., Trop, J., Glen, J., and O'Neill, J. (2007). *Tectonic Growth of a Collisional Continental Margin: Crustal Evolution of Southern Alaska*.

Sandwell, D., Mellors, R., Tong, X., Wei, M., and Wessel, P. (2011). Open radar interferometry software for mapping surface deformation. *EOS, Trans. AGU*, 92(28):234–234.

Schneider, D., Bartelt, P., Caplan-Auerbach, J., Christen, M., Huggel, C., and McArdell, B. W. (2010). Insights into rock-ice avalanche dynamics by combined analysis of seismic recordings and a numerical avalanche model. *Journal of Geophysical Research: Earth Surface*, 115(F4).

Singhroy, V., Mattar, K., and Gray, A. (1998). Landslide characterisation in canada using interferometric sar and combined sar and tm images. *Advances in Space Research*, 21(3):465–476.

Toney, L. and Allstadt, K. E. (2021). lsforce: A python-based single-force seismic inversion framework for massive landslides. *Seismological Society of America*, 92(4):2610–2626.

Toney, L., Fee, D., Allstadt, K. E., Haney, M., and Matoza, R. S. (2020). Re-

constructing the dynamics of the highly-similar may 2016 and june 2019 iliamna volcano, alaska ice–rock avalanches from seismoacoustic data. *Earth Surface Dynamics Discussions*, pages 1–32.

Toney, L., Fee, D., Allstadt, K. E., Haney, M. M., and Matoza, R. S. (2021). Reconstructing the dynamics of the highly similar may 2016 and june 2019 iliamna volcano (alaska) ice–rock avalanches from seismoacoustic data. *Earth Surface Dynamics*, 9(2):271–293.

van Driel, M., Krischer, L., Stähler, S. C., Hosseini, K., and Nissen-Meyer, T. (2015). Instaseis: Instant global seismograms based on a broadband waveform database. *Solid Earth*, 6(2):701–717.

Wang, K., Xu, X., and Fialko, Y. (2017). Improving burst alignment in TOPS interferometry with bivariate enhanced spectral diversity (BESD). *IEEE Geoscience and Remote Sensing Letters*, 14:2423–2427.

Xie, J., Chu, R., and Ni, S. (2020). Relocation of the 17 june 2017 nuugaatsiaq (greenland) landslide based on green's functions from ambient seismic noises. *Journal of Geophysical Research: Solid Earth*, 125(5):e2019JB018947.

Xu, Y., George, D. L., Kim, J., Lu, Z., Riley, M., Griffin, T., and de la Fuente, J. (2021). Landslide monitoring and runout hazard assessment by integrating multisource remote sensing and numerical models: an application to the gold basin landslide complex, northern washington. *Landslides*, 18(3):1131–1141.

Yamada, M., Matsushi, Y., Chigira, M., and Mori, J. (2012). Seismic recordings of landslides caused by typhoon talas (2011), japan. *Geophysical Research Letters*, 39(13).

Yonezawa, C. and Takeuchi, S. (2001). Decorrelation of sar data by urban damages caused by the 1995 hyogoken-nanbu earthquake. *International Journal of Remote Sensing*, 22(8):1585–1600.